APPENDIX

Report on instrument's tests

Based on runs:

April 27-30 2020	Focal reducer + T193 Guiding
July 6-9 2020	Blue Imaging
October 19-20 2020	Blue Spectroscopy + Red Imaging
November 23-25 2020	Blue Spectroscopy + Red Imaging
December 8-9 2020	Red Spectroscopy
December 26 2020	N&S Red Spectroscopy
January 4-5 2021	Transients + ETC populating
February 12-15 2021	ETC populating + Command Control tests + quick-look tool test
April 2-5 2021	Night-time data reduction process
July 5-6 2021	FOCUS procedures + new command control
September 6-7 2021	Internal guiding tests
December 6-8 2021	Internal guiding tests + ToO procedures

Version : 08/04/2022

This document summarizes several tests we conducted with the instrument and which were used in the primary cookbook.

Table des matières

Appendix I : Populating the ETC tool

We give in this section the list of observations used to populate the ETC tool. Table B1 gives also the list of transient identifications we could achieve with MISTRAL spectra (and the associated Astronomer Telegram number when published).

Table B1 List of MISTRAL spectral observations used to populate the ETC tool and transient identification when available.

Name	V mag	shape	VPH	Exp. time	Class
Stars					
HD30614	4.29	point	blue	615	O star
HD21428	4.73	point	blue	165	B star
Hiltner 600	10.44	point	blue	300	B star
Zeta Cassiopée	3.66	point	red	5	B star
HD34989	5.8	point	red	10	B star
HD1544	8.12	point	red	10	B star
Hiltner 600	10.44	point	red	300	B star
Feige 15	10.19	point	blue	600	A star
Feige 15	10.19	point	red	600	A star
HD20041	5.79	point	blue	165	A star
HD30034	5.38	point	blue	165	F star
HD55730	5.70	point	blue	165	G star
HD19445	8.06	point	red	120	G star
HD27971	5.28	point	blue	115	K star
sp13lac	5.08	point	blue	5	K star
T Tauri	10.12	point	red	300	K star /TTauri
HD42471	5.77	point	blue	115	M star
Star in n0517 galaxy cluster	16.55	point	blue	3600	Star
Sh2_252A los star	13.67	point	red	600	star
Mars	-2.28	point	blue	2	Solar spectra
Parthenope	9.37	point	blue	300	Solar spectra
Sh2_252A central object	12.67	point	red	1800	YSO
Transients					
at2021fv	17.86	point	blue	2400	SN Atel #14304
at2020aaue	19.5	point	red	3600	Transient

at2020abtd	16.15	point	red	3600	Transient
atlasbgux	18.4	point	red	2700	Transient
at2020abfa	18.6	point	red	3600	SN Atel #14263
at2020abqq	18.6	point	red	2400	SN Atel #14263
gaia20flc	14.5	point	red	1200	Be Star Atel #14263
gaia20fnu	17.65	point	red	3600	SN Atel #14263
gaia20fpd	18.2	point	red	3600	SN Atel #14263
at2020aafw	18.5	point	blue	3600	Transient
at2020aaue	19.5	point	blue	6150	Transient
at2020aafw	18.5	point	blue	3600	Novae Atel #14215
gaia20ffy	18.8	point	blue	1800	Transient
at2020aaxq	19.54	point	blue	7500	Transient
at2020aaxi	14.9	point	blue	600	Transient
Galaxies					
WISEA J025857.96+095748.3	16.5	extended	red	3600	Galaxy
WISEA J082336.76+042302.4	15.5	extended	red	60	Galaxy
KUG 1010+362	15.3	extended	red	3600	Galaxy
CGCG 064-083	15.	extended	red	3600	Galaxy
Host of gaia20ffy	18.8	extended	blue	1800	Galaxy
Host of at2020aauz	18.15	extended	blue	3600	Galaxy
WISEA J013933.81+344726.0	16.5	extended	blue	7500	Galaxy
Xclass 102	15.09	extended	blue	3600	BCG galaxy
Xclass 3091	14.37	extended	blue	2700	BCG galaxy
Xclass 3091 2	15.4	extended	blue	2700	Second galay of Xclass 3091
NGC1275	11.9	extended	red	1200	BCG galaxy
NGC4330	12.5	extended	blue	3600	Galaxy
NGC4151	10.8	extended	blue	660	AGN

Appendix II: wavelength calibration stability

We give in Figs. A1 and Tab. B2 the list of wavelengths used for spectral calibration.

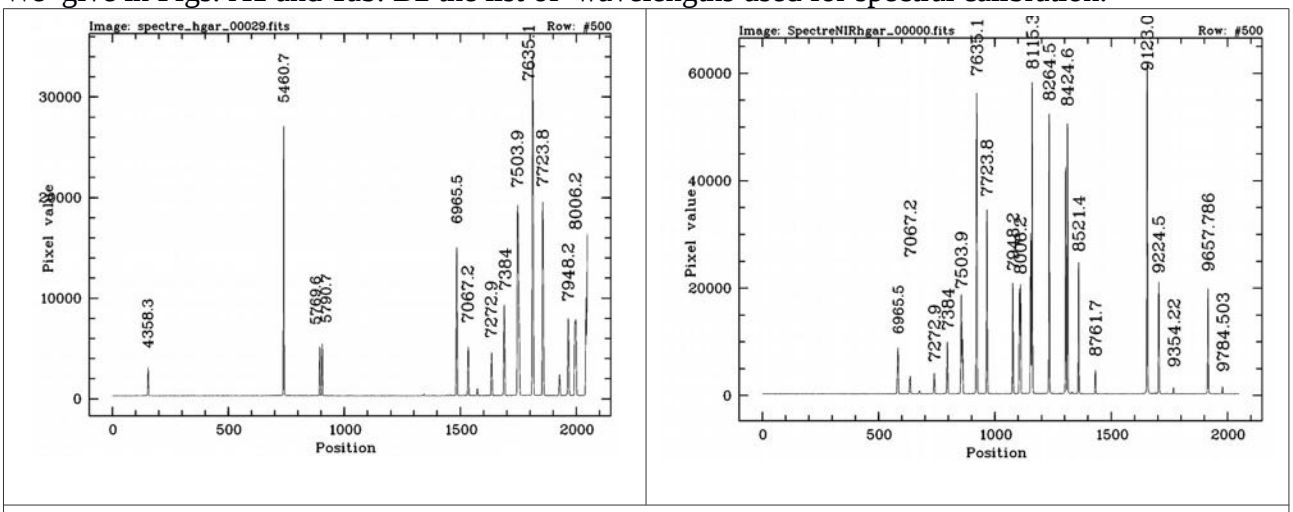

Fig. A1: Calibration spectra for HgAr lamps with the blue (left) and red (right) dispersers.

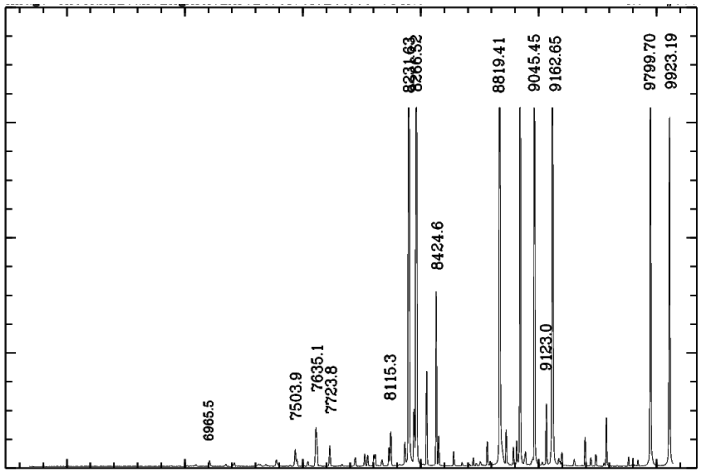

Fig. A1: Calibration spectra for HgArXe lamps for the red disperser.

2536.5	4521.86	4923.15	7119.60	7948.18	9045.4
2967.3	4609.57	5460.73	7147.04	7967.34	9123.0
3021.5	4624.2	5769.60	7272.93	8057.26	9162.65
3131.6	4657.90	5790.66	7311.70	8061.34	9224.50
3341.5	4690.97	6416.30	7353.30	8115.31	9657.78
3650.15	4698.04	6318.06	7383.98	8231.63	9784.50
4046.56	4734.15	6472.84	7509.62	8264.52	9799.70
4158.59	4764.87	6677.28	7584.68	8266.52	9923.19
4200.68	4792.62	6728.01	7635.11	8280.12	10838.4
4259.36	4807.02	6871.30	7642.02	8424.65	
4300.10	4829.71	6911.23	7723.98	8521.44	
4358.33	4843.29	6965.43	7802.65	8667.94	
4510.73	4916.51	7067.22	7887.40	8819.41	

Table B2: list of line wavelengths (in Angströems) used for the spectral calibrations (HgArXe)

Blue dispersor wavelength calibration stability with HgAr lamps

It is crucial to know how frequently a wavelength calibrations has to be performed in order to have the right wavelength determination of spectral features in a given spectrum. For this, we have taken 24 spectroscopic calibrations (twelve groups of two calibrations) over three nights in November 2020 at various telescope positions. For each of these exposures we first identified the same strong spectral lines (5460.7A, 6965.4A, 7503.9A, 7635.1A, 7723.8A), before the final identification of all the lines detected in the HgAr lamps was performed automatically.
This allows first to check the stability of the starting and ending wavelengths, and the value of the pixel step for quasi simultaneous calibration exposures, that is made at the same instrument position. Figure A2 shows that the precision is most of the time better than 30 km/s for the blue extremity and 15 km/s for the red extremity. The wavelength step is typically varying by 0.05 km/s.

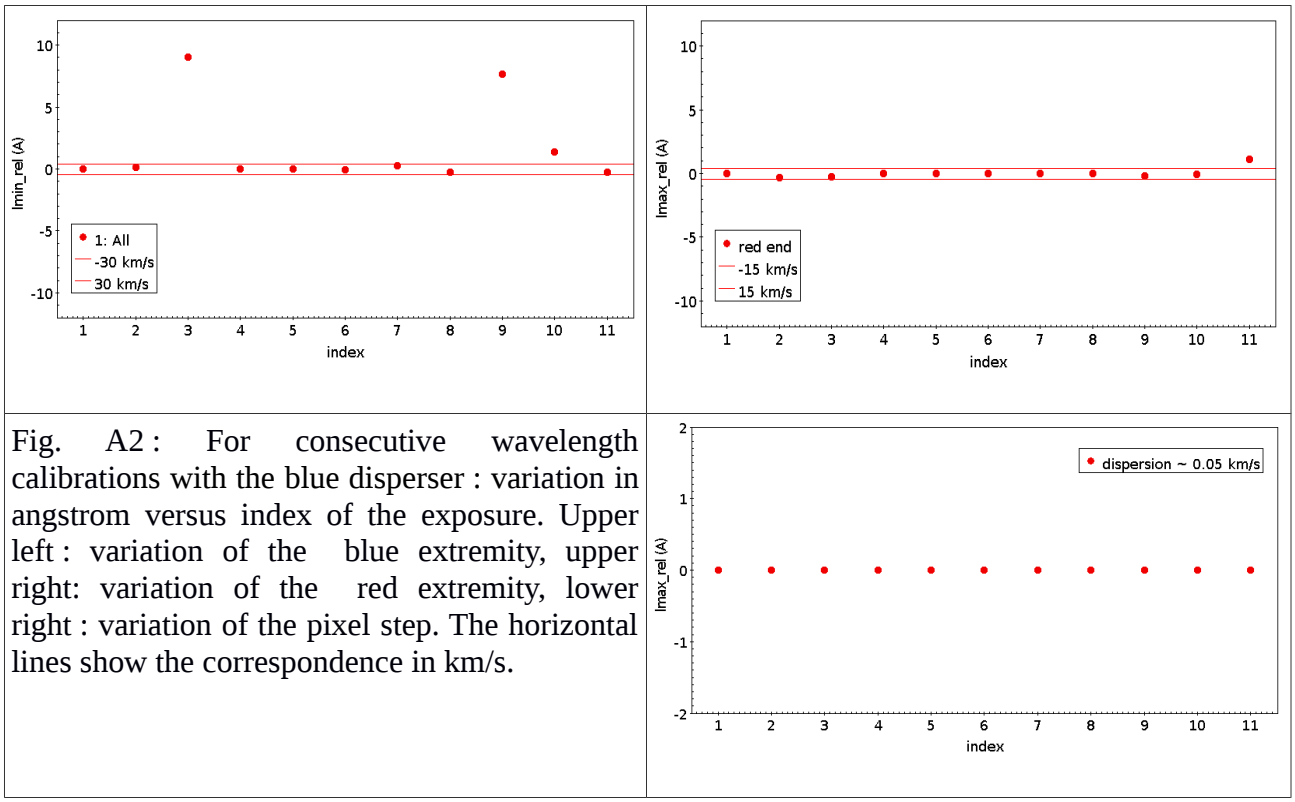

Fig. A2 : For consecutive wavelength calibrations with the blue disperser : variation in angstrom versus index of the exposure. Upper left : variation of the blue extremity, upper right: variation of the red extremity, lower right : variation of the pixel step. The horizontal lines show the correspondence in km/s.

Corresponding results for non consecutive exposures, at different instrument positions, are shown in figure A3. For non consecutive exposures, an accuracy most of the time better than 200 km/s is reached for the red side and is between 200 and 400 km/s for the blue side. The pixel step is typically varying by 0.1 km/s. For science goals requiring velocities better than 400 km/s it seems therefore necessary to get wavelength calibration exposures at the same instrument's position than for the science exposure, specially for the blue end (fewer calibration lines available).

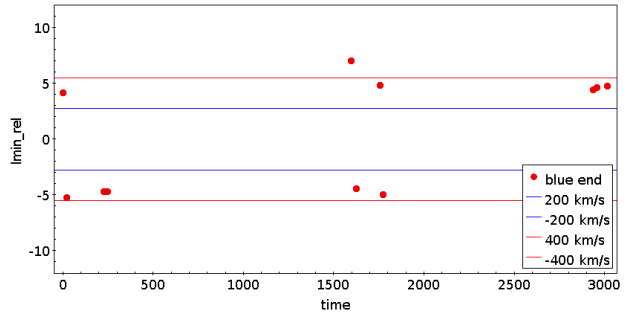

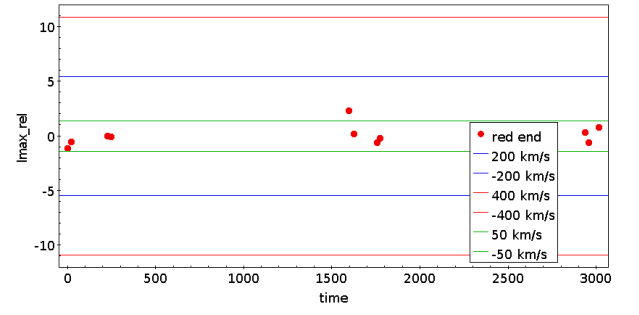

Fig. A3 : for non consecutive lambda calibrations with the blue disperser : variation in angstrom versus index of the observation date (in min). Left : variation of the blue extremity (in A), Right: variation of the red extremity (in A).

Red dispersor wavelength calibration stability with HgAr lamps

Similar investigations have been made for the red disperser. Thirteen wavelength calibration exposures have been made over two nights at different telescope positions. Each exposure was first wavelength calibrated with the strong 6965.4A, 7635.1A, 8115.3A, 9123.0A, 9657.8, and 9784.5A lines before the final calibration was achieved with all the available lines. Figure A4 shows that non consecutive exposures are stable with less than 100 km/s shifts both at the red and the blue end. The pixel step is varying typically by 0.05 km/s. If the science goal requires an accuracy better than 100km/s, it is therefore necessary to get wavelength calibration exposures at the same instrument's position where the science exposure was obtained

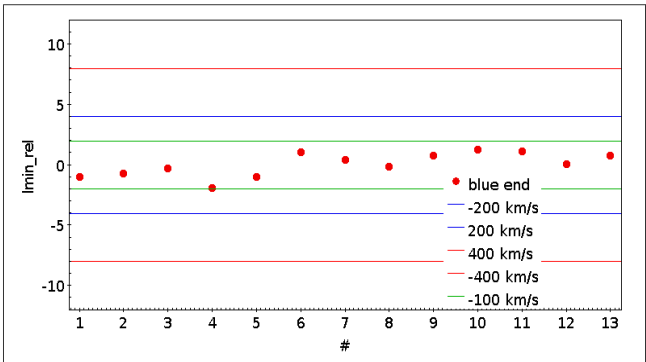

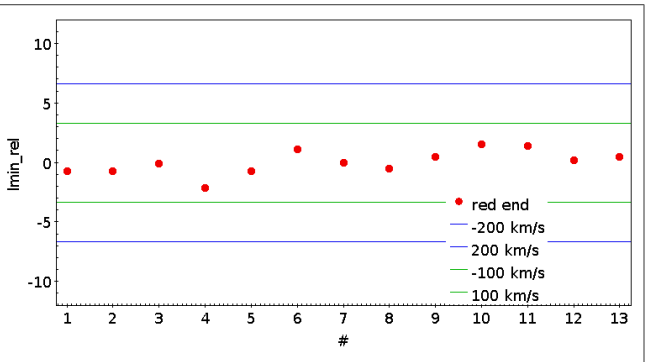

Fig. A4 : For non consecutive lambda calibrations with red dispersor: variation in A versus observation index. Upper left : variation of the range blue end (A), upper right: variation of the range red end (in A), lower right : variation of the step (in A). The horizontal lines show the correspondances in km/s.

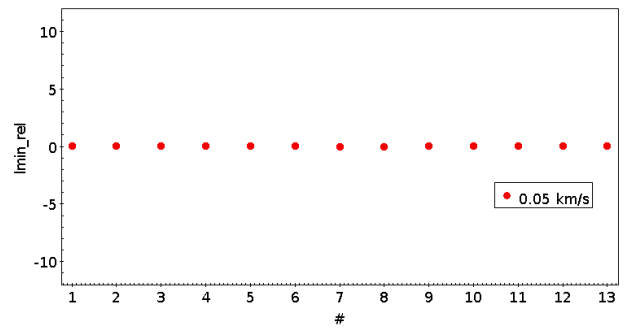

Blue and Red disperser wavelength calibration stability with HgArXe lamps

The addition of a Xe lamp modifies the previous values. Similar tests were made over a full night (10 wavelength calibrations, different telescope positions). The results are summarized in Table B3.

Table B3: Summary of variations (over a full night) of the starting and ending wavelengths of the blue and red dispersers. Values are given for the HgAr and HgArXe lamp combinations.

	Blue disperser		Red disperser	
	Blue end	Red end	Blue end	Red end
HgAr	374 km/s	34 km/s	50 km/s	31 km/s
HgArXe	274 km/s	50 km/s	23 km/s	11 km/s

Blue and red disperser common wavelength range

Another way to estimate the velocity accuracy of our spectral observations is to use the common wavelength range between the blue and red disperser. In this framework, we observed the Gaia20ffy transient host galaxy with both the blue and red disperser (in November and December 2020) and extracted the common spectral domain (~6000-8000A : see Fig. A5). Selecting the [OIII] doublet, the velocity difference between the two spectra is of the order of 150 km/s, in good agreement with the uncertainties shown before by the edges of the blue and red dispersers.

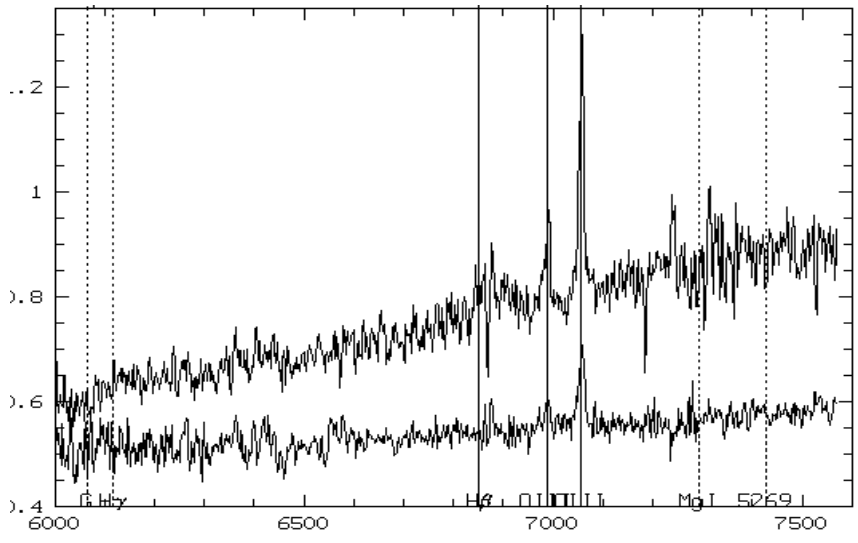

Fig. A5 : red (lower spectrum) and blue (upper spectrum) disperser spectra of the Gaia20ffy transient host galaxy (at z=0.4094).

Appendix III: Magnitude completeness

This estimate was performed using the Xclass3091 field (already imaged by the SDSS), where we separately detected pointlike (stars) and extended (galaxies) objects. This was done with Sextractor (Bertin & Arnouts 1995) at the 3sigma level. Several successive images were observed under similar seeings of 2arcsec in the g', r', i', z' and Y band filters, giving us different depths for each filter. This cluster of galaxies was already imaged by the SDSS survey with the same g', r', i', z' filters. SDSS images can therefore serve as references because they are deeper than the MISTRAL ones, with a better seeing, and with a better instrumental spatial resolution.

After classical reduction (skyflats and offsets), objects were then detected in each of these images and identified with corresponding SDSS objects (see fig. A7 for an exemple of g'-band MISTRAL and SDSS image). Figure A6 then shows the percentage of SDSS detected objects as a function of the magnitudes.

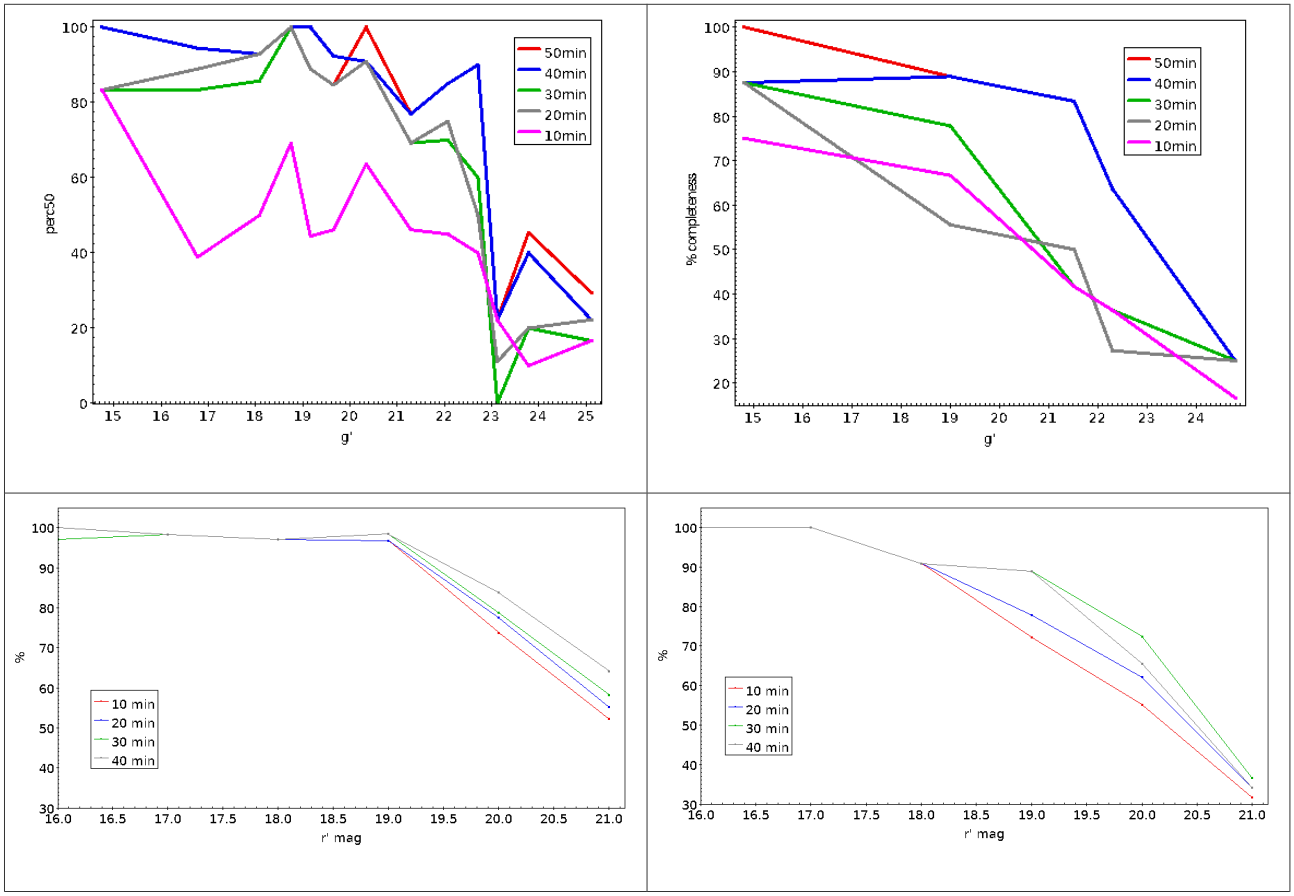

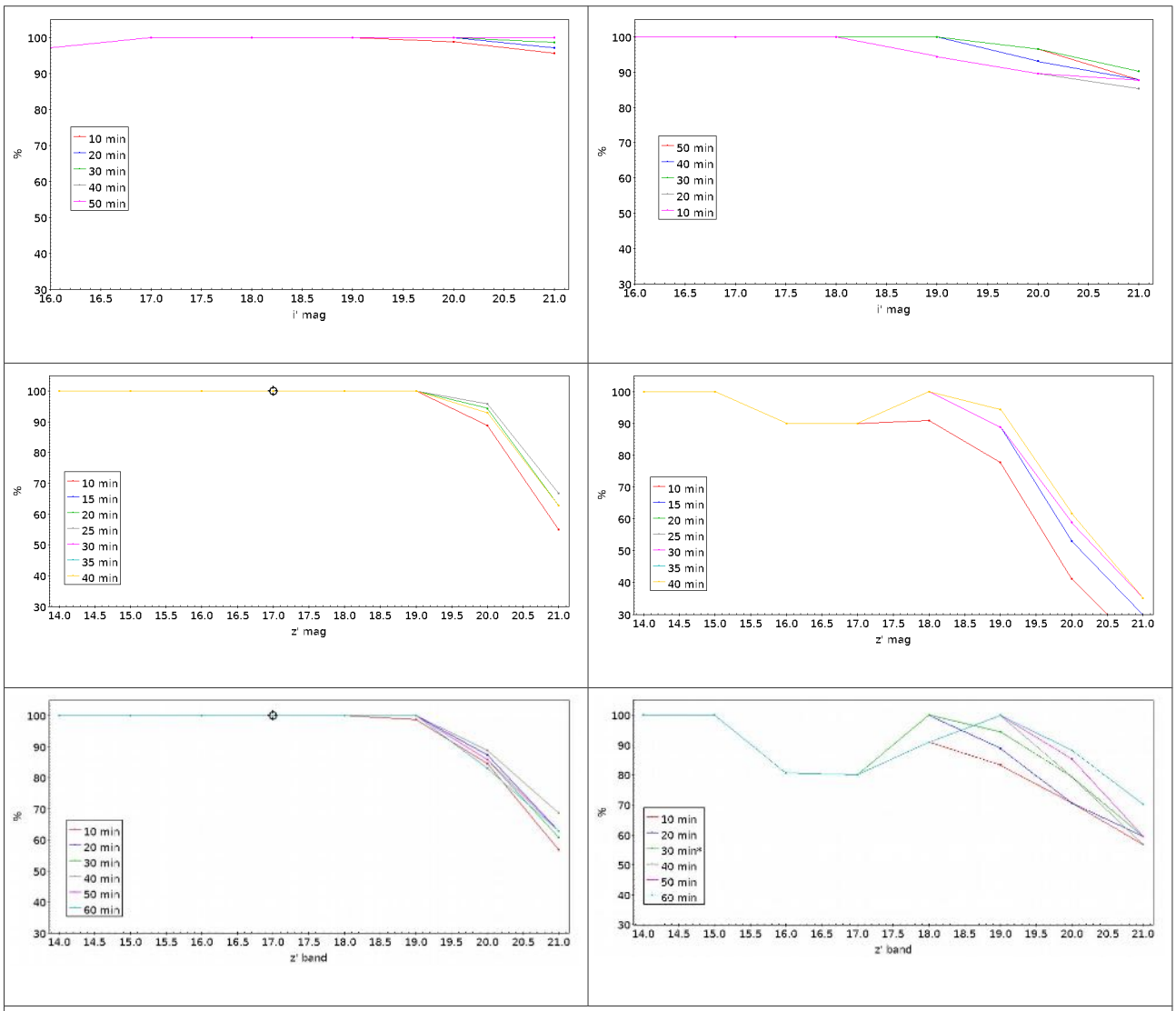

Fig. A6 : % of MISTRAL re-detected SDSS objects in the g', r', i', z', Y bands (top to bottom) for different MISTRAL exposure times vs magnitude. Left : pointlike, Right : extended objects.

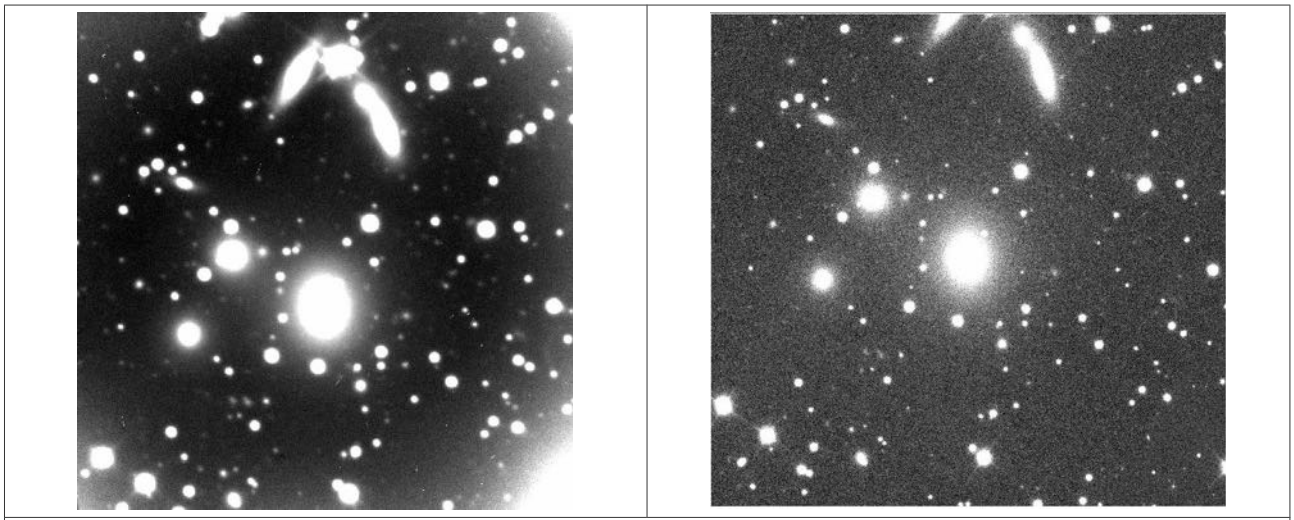

Fig. A7 : Left: g'-band MISTRAL (50min exposure), seeing~3 arcsec, Right : g'-band SDSS.

Appendix IV: Magnitude uncertainties

Several uses of MISTRAL (e.g. photometric redshifts) require the knowledge of the accuracy of the magnitudes. To estimate this, we used deep exposures of the Xclass3091 cluster of galaxies. We identified objects along this line of sight, observed with the g', r', i', z' and Y band filters, with the SDSS g', r', i', and z' catalogs. Y band MISTRAL objects were compared with z' band SDSS detections. Fig. A8 gives the resulting uncertainty (1sigma level) between the MISTRAL and SDSS measurements as a function of magnitude. We note that for the bright magnitudes, objects are saturated, explaining the higher uncertainty values.

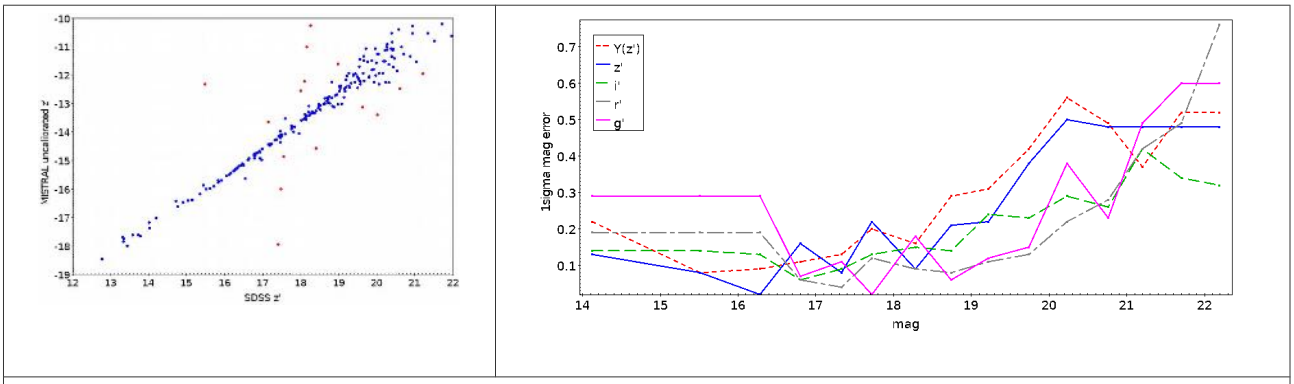

Fig. A8 Left: direct comparison between MISTRAL and SDSS z' magnitudes along the line of sight of the Xclass3091 cluster of galaxies. The red dots are wrongly identified objects. Right : 1sigma uncertainty versus g', r', i', z' magnitudes.

Appendix V : Detection of point-like objects embedded in extended sources : the YSO case

« Young Stellar Objects » are proto-stars embedded in more or less opaque HII regions. They are, by definition, quasi impossible to detect within the optical bands g', r', i', and even z' because their flux is absorbed by the diffuse medium around them. However, they are more easily detected in NIR bands like J, H, or K because the absorption is smaller in the IR. MISTRAL provides a Y band filter, intermediate between optical and NIR wavelengths, and we have therefore compared MISTRAL Y-band imaging with 2MASS public data of the HII region Sh2-252A. Six 5min long Y-band images have been obtained with MISTRAL in imaging mode. After standard reduction (offsets & Skyflats) and astrometric calibration (with the SIMBAD tools), we have correlated the positions of the YSO detections with the ones provided by the 2MASS survey. Fig. A9 shows the comparison between MISTRAL Y-band and 2MASS J-band images. MISTRAL 20min exposures appears long enough to redetect all the embedded objects visible in J band in the 2MASS survey. We note that nearly none of them appear in r', [OIII] or Hα bands.

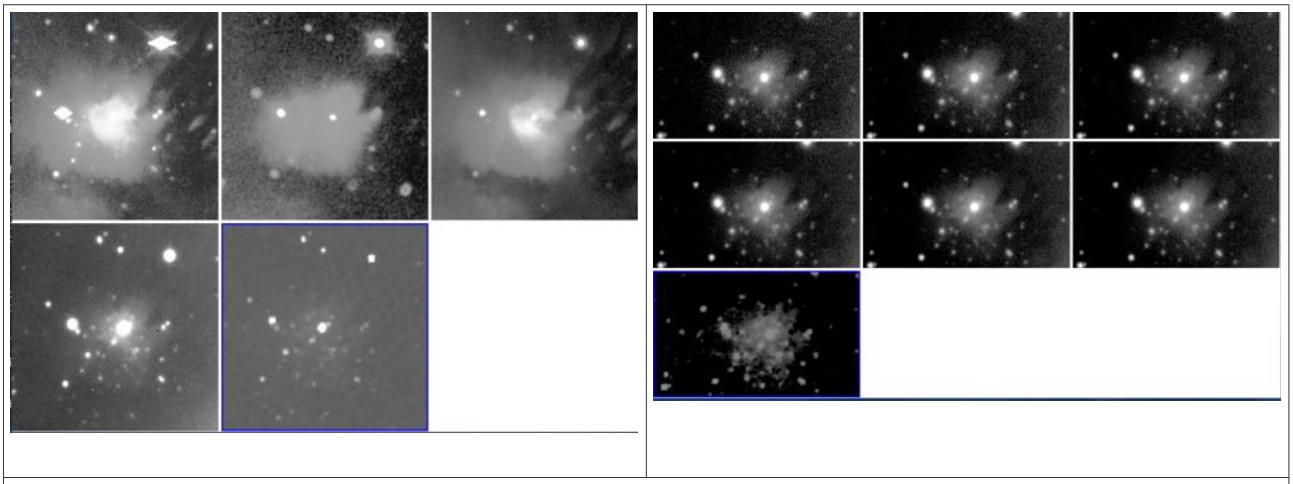

Fig. A9 : Left : from left to right and top to bottom : MISTRAL images of Sh2-252A in r', [OIII], Hα, Y, and the 2Mass J band. Right : from left to right and top to bottom : MISTRAL images of Sh2-252A in Y band with 5, 10, 15, 20, 25, and 30 min exposures and the 2MASS J band. Cuts used are ds9 zscale+histogram to enhance the faint features.

Appendix VI : Offset stability versus reading mode

Fig. A10 shows the offset level variation across the CCD, line per line (averaged over 10 lines). This variation is weaker than the one percent level for both rapid and slow reading mode. For basic uses, this opens the possibility to simply subtract a constant value (equal to 302) from the science images, instead of a median of several offsets.

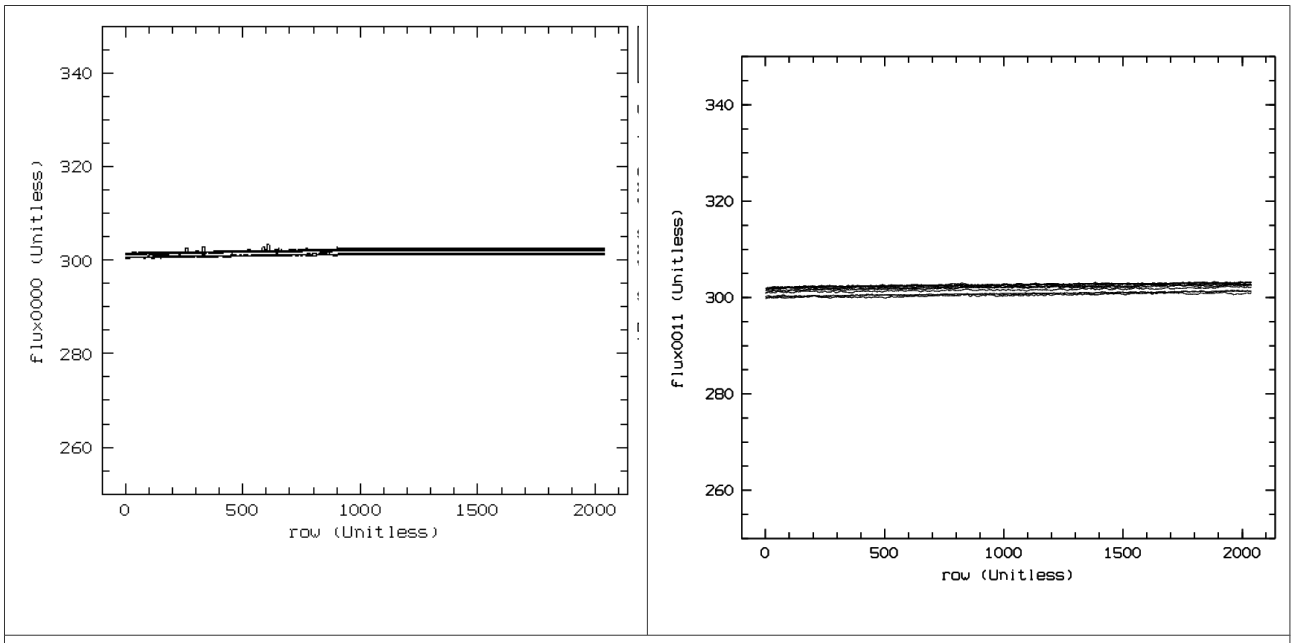

Fig. A10 Offset mean pixel flux per line as a function of the line number. Left : slow reading mode. Right : rapid reading mode.

Appendix VII : Imaging flatfields

One of the key steps of the imaging process is the correction of the CCD response variation across its area, known as the flatfielding process. This simply consists in observing a uniform light source and then deducing the CCD response variation. This uniform light source can consist in a white screen enlighted by some continuous lamps (domeflats), or in the sky itself before the dark night, when stars are still below the sky level (skyflats). The T193 telescope has no flatfield screen in the dome, so the best way to get flat fields is to use the sky technique.

We however tested the quality of a domeflat using the T193 dome itself as flatfield screen. For this, we observed flatfields in g', Hα and Y bands, alternatively on the dome (to the left of the trap, at an elevation of 60deg) and on the sky. For each filter, we first subtracted a median offset and then normalized the flatfields by their mean level. Finally, for a given filter, we simply divided the domeflat by the skyflat in order to evaluate the percentage of variations between the two flatfield estimates across the CCD's 5'x5' central field. Results are given in Fig. A11. Red contours in fig. A11 vary from 89 to 100 % by steps of 1 %. Blue contours vary from 101 to 128 % by steps of 2 %. We see that skyflats are most of the time less intense than the domeflats on the edges of the field. In the field center, they are more intense, especially in the Y-band. The g'-band also shows a peculiar behaviour : vertical structures are appearing in the domeflats, probably corresponding to the dome frame itself. Differences between dome and skyflats can therefore be at the 20 to 30 % level, potentially inducing important differences in astronomical objects photometry.

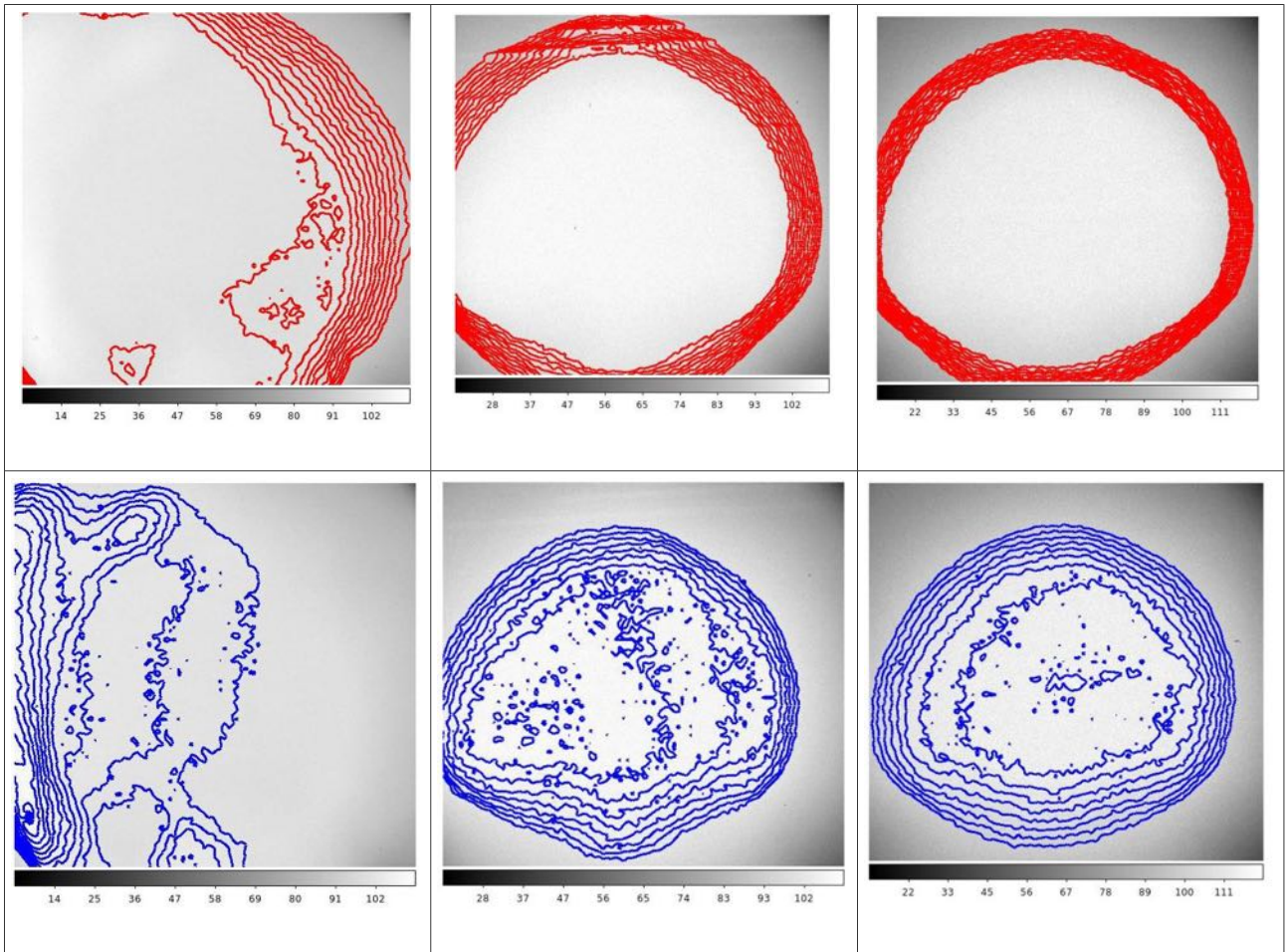

Fig. A11 : percentage differences between dome and skyflats in g' band (left), Hα band (center), and Y-band (right) . Red contours (upper figures) vary from 89 to 100 % by steps of 1 %. Blue contours (lower figures) vary from 101 to 128 % by steps of 2 %.

Appendix VIII : Reducing fringing in spectroscopic data

We have investigated the fringing signal periodicity as a function of the CCD line in order to evaluate how it can be removed. For each of the spectral flatfield exposures, with the red grism, we extracted the signal (including therefore the fringing signal) within the 500 last pixels toward the CCD red edge, for each CCD line. This corresponds approximately to the 9000-10000 A wavelength range, the place where the fringing is the strongest.
We clearly detect a sinusoidal signal and we have computed its periodicity, computing its Fourier transform. Fig. A12 then shows the fringing signal periodic variation as a function of the CCD line. The period clearly changes across the CCD y-direction, sometimes by several pixels between two successive lines. This small scale variation induces variations of the x-pixel including the local fringing maxima, of the order of the signal period itself. This is illustrated in Fig. A12 where we see that the x coordinate of the fringing maximum can vary by four pixels over six lines. The standard sky subtraction technique assumes that the sky parts immediately adjacent to the science object are identical to the sky under the object. This is obvioulsy wrong in the present case. It is therefore mandatory to estimate the « sky » under the object exactly at the same place as the object itself to get rid of the fringing.

In principle, this is possible if the fringing variation with time is weak. In order to check this point, we also show in fig. A12 (upper right) that the fringing spatial frequency variation as a function of the CCD line is only weakly dependent on time. Over a two night period, an exposure taken at a given « t » time has the same fringing pattern whatever « t ». This is not, however, taking into account the sky (atmospheric lines) time-dependant variation itself, so the « sky » must be extracted as close as possible in time to the « object » signal. This is possible using the classical Nod&Shuffle technique consisting in alternatively observing object and sky at the same place (see e.g. http://www2.gemini.edu/node/10627).

We tested a manual version of this technique with MISTRAL, simply consisting in making relatively short successive exposures at two different places of the object within the slit in a ABAB observing mode. The object is put at position A for the first exposure. Then the object is put at position B for a second exposure, then, position A again for a third exposure, ..etc... We tested the technique for two objects : a V~12.5 isolated YSO protostar (ic348lrl20 with 3min individual exposures), and a redshifted V~17.5 emission line galaxy ar z~0.43 (with 5min individual exposures). We adopted a distance of 60 pixels along the slit between positions A and B. We summed a total of 30 minutes exposure for both objects. These objects were also observed for the same duration during the same night with the regular technique (two 15min exposures with objects remaining at the same place within the slit).
In the first case, the sky under the object in an A exposure was measured at the same place in a B exposure and vice versa. In the second case, the sky under the object was measured just below and above the object in the same exposure. Results of the two object's spectra extraction is shown in Fig. A13. Blue-wards of 9300A, both techniques provide very similar results. Red-wards of 9300A, the noise is reduced by a factor of two for the YSO observation with the ABAB technique. However, this is not sufficient to make the Paschen lines to appear. For the galaxy, the H line is only seen with the ABAB technique.

The ABAB technique is however very expansive in terms of overheads.
- For a 30min science exposure, classical technique adds 80sec of reading time (4% of total time).
- The ABAB technique adds 240sec and 600sec of reading time for individual exposures of 5min and 3min. We must also add the required time to shift the object between positions A and B (guiding

star off, shift, guiding star on), of the order of 30sec per shift. This represents in total respectively more than 20 % and nearly 50 % of the science exposure time.

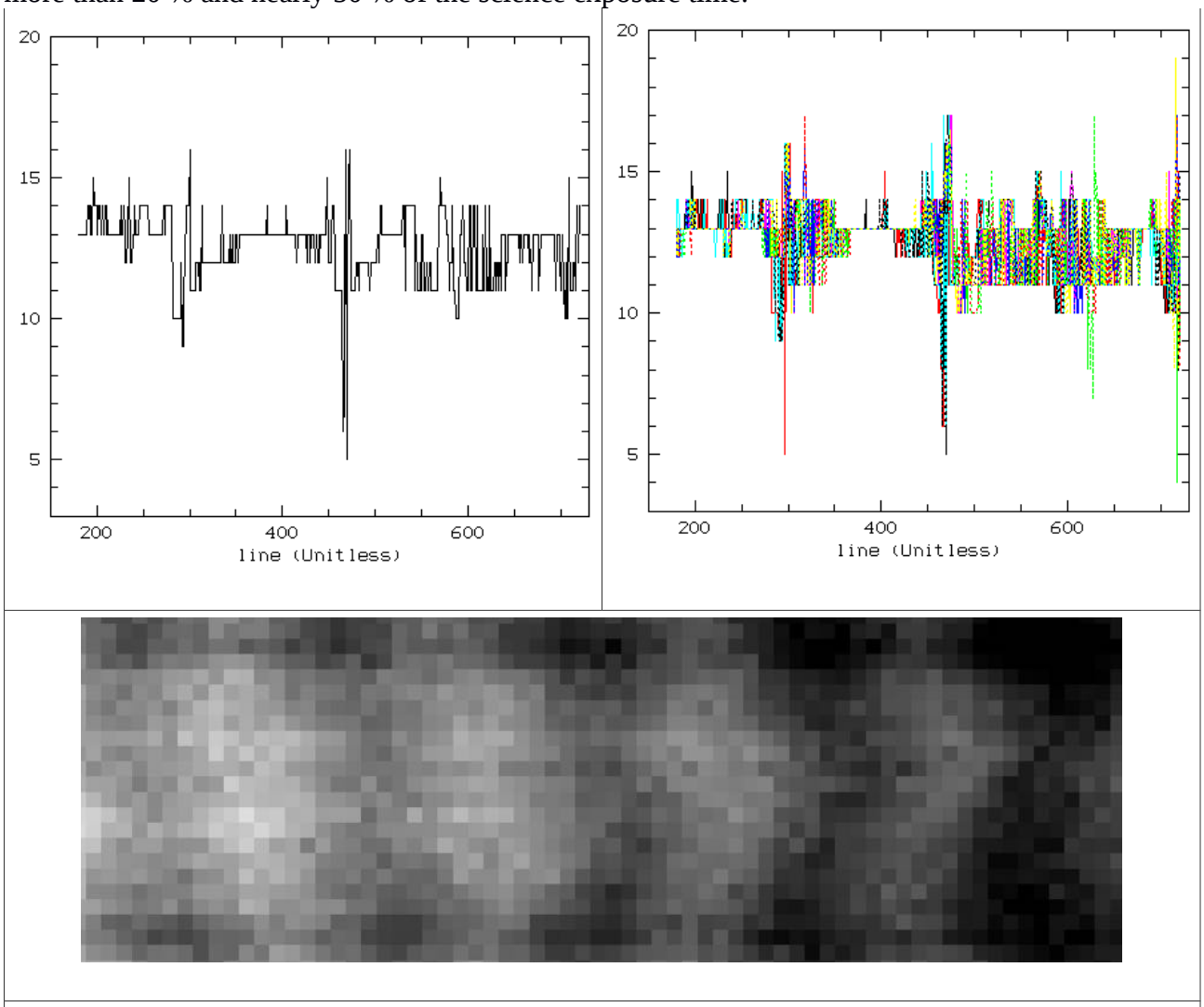

Fig. A12 : Upper left : fringing signal period (in pixels) as a function of the CCD line (in pixel) for the first spectral flatfield exposure of the December 2020 run. Upper right : superposition of the same results for the twelve flatfield exposures of the run. Lower part : zoom on the 2D fringing signal in a red part of the first spectral flatfield exposure of the December 2020 run.

In conclusion, this ABAB technique can provide significantly better sky subtraction in the (rare) cases where objects include interesting lines red-wards of 9300A, at the cost however of a large increase of the overheads and a complicated data reduction (as no automated procedure is provided at the moment to deal with this kind of observing mode). This mainly concerns galactic objects for Paschen lines or redshifted objects.

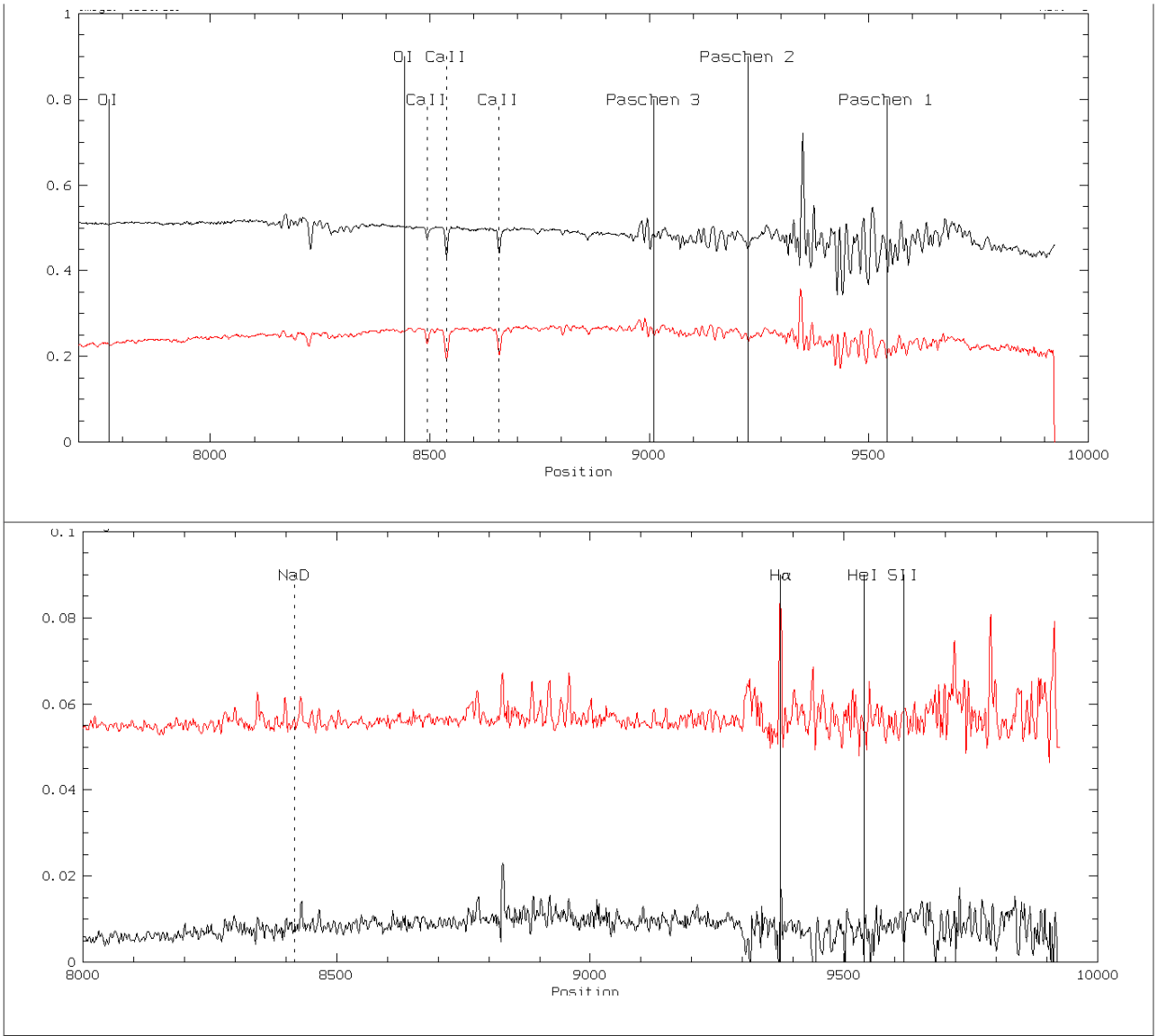

Fig. A13 : Upper figure : galactic YSO. Lower figure : z~0.43 emission line galaxie. Typical absorption lines are shown for the YSO and the Hα line is shown for the galaxy.

Appendix IX : general object bestiary

Extended galactic objects

We present in this section observations of the HII region Sh2-252A. Its size is well adapted to the MISTRAL field of view. Figure A14 shows [OIII] (40minutes exposure), Hα (50min exposure) and trichromic r' (20min exposure), [OIII], Hα color image.

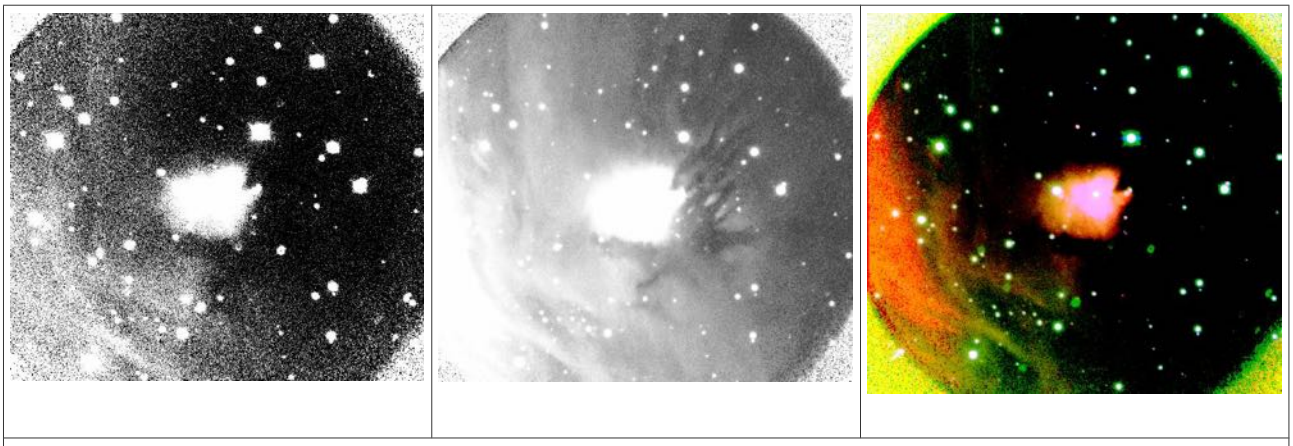

Fig. A14 : Sh2-252A images : left : OIII (40min), middle : Halpha (50min), right : trichromy r' (blue channel), Halpha (red channel), OIII (green channel, binned 2x2).

We note that the [OIII] band is quite shallow showing that a 40minutes exposure was not sufficient to reach the Hα depth.

Spectra of extended galactic objects

The MISTRAL spectral resolution does not allow to reach velocity fields with an accuracy better than a few dozen of km/s, depending somewhat on the spectral domain. However, large expansion velocity objects such as Supernovae remnants can be followed. In this framework, we got a single slit spectrum of the Crab Nebula. Fig. A15 shows the resulting spectrum and the corresponding velocity field.

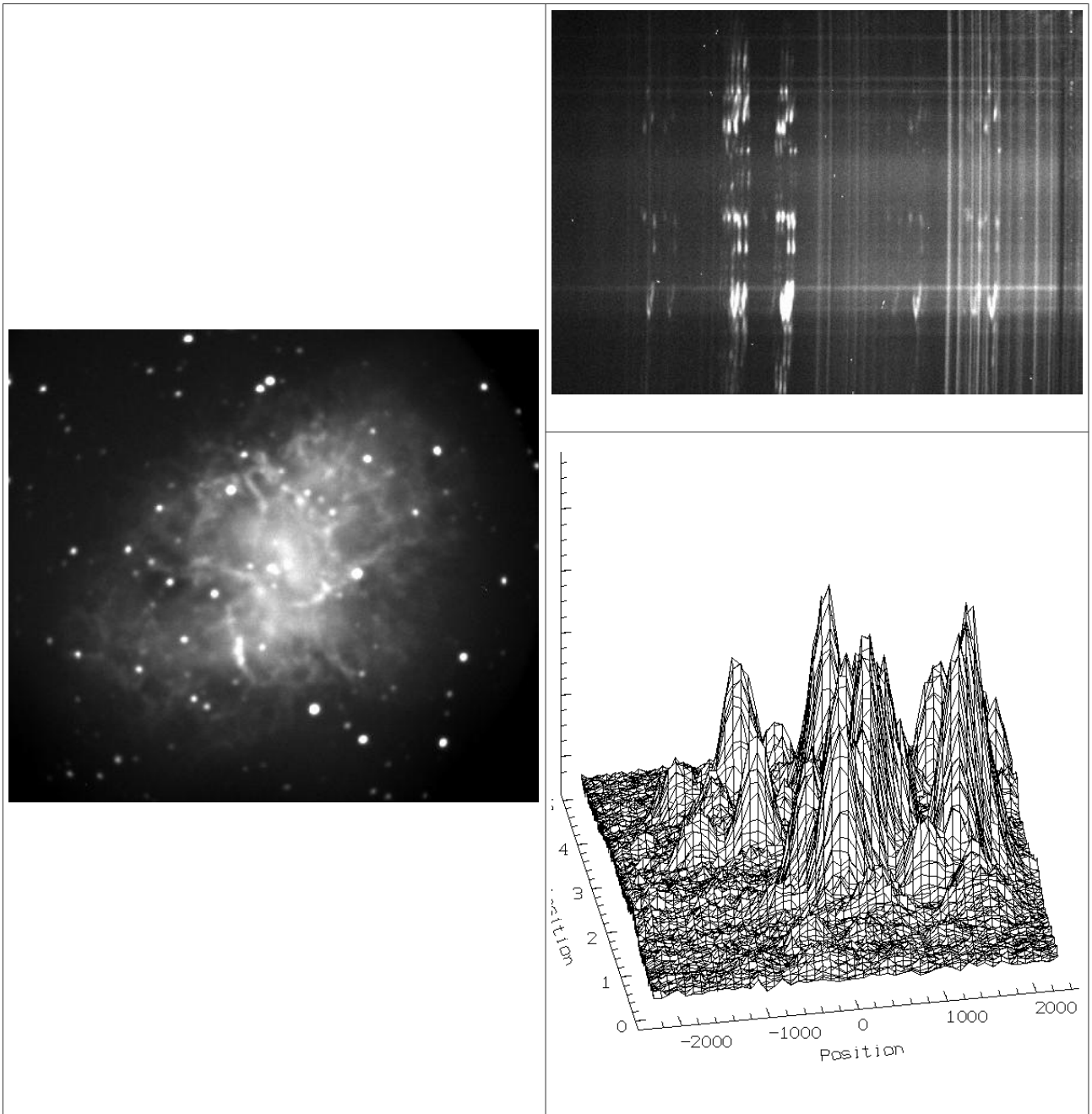

Fig. A15 Left : 60sec r' band image of the Crab nebula. Upper right : 900sec 2D image of the Crab nebula observed with the red disperser and zoomed around the Halpha/SII lines. Lower right : velocity field (relative velocity in km/s) in x and spatial position along the slit (in arcmin) in y. The z axis is the Hα line intensity in arbitrary unit.

Stellar spectra

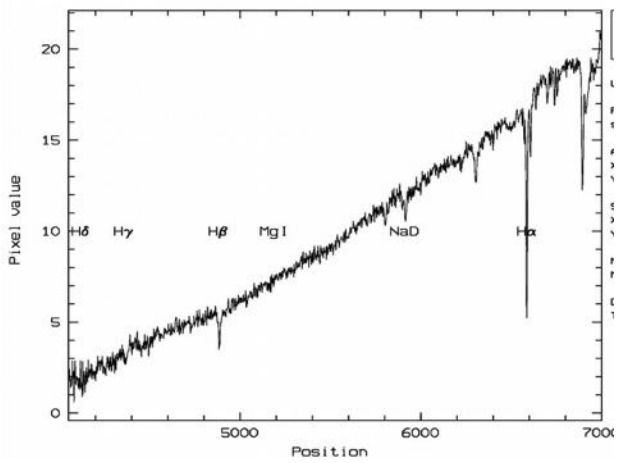

Sh252 central object, Young Stellar Object candidate, exp. Time : 600sec, V=13.7

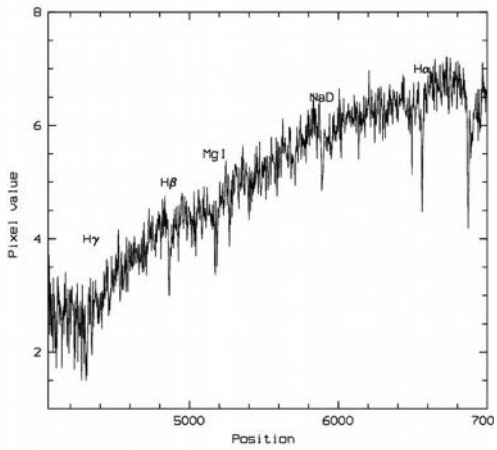

Astéroid : Parthénope, exp. Time : 300sec, V=9.4

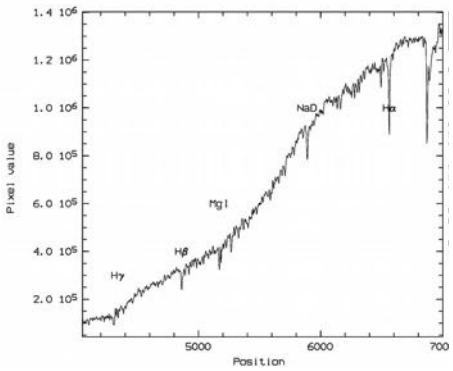

Mars, Exp. Time : 2sec, V=-2.3

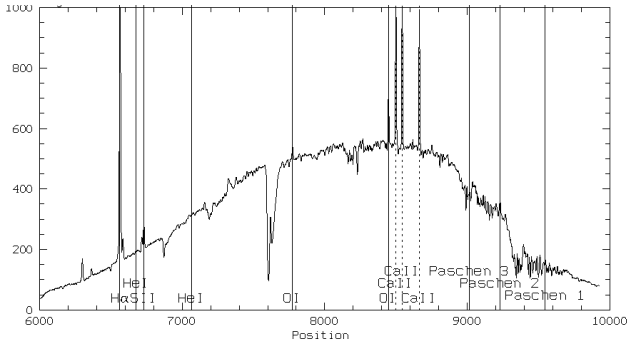

T-Tauri, exp. Time : 300sec, V=10.1

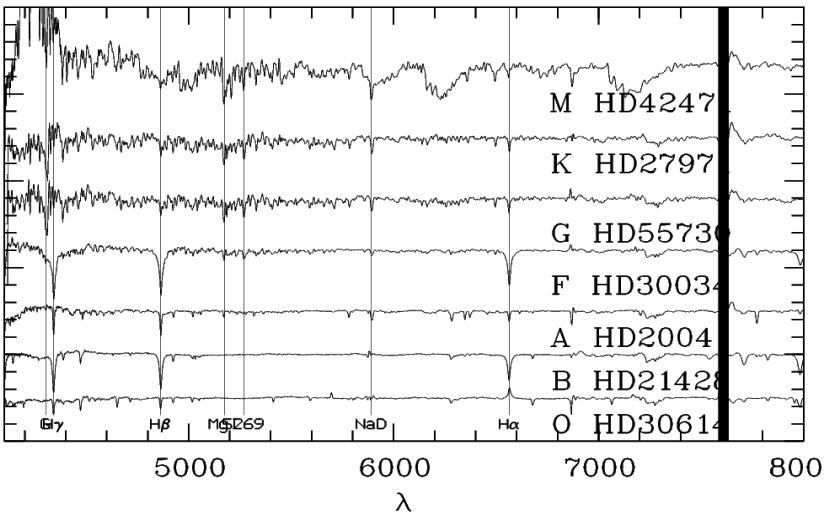

Fig. A16 : general stellar bestiary. Sh2_252A YSO, Parthenope asteroid, Mars, T-Tauri, bright OBAFGKM normalized stars (arbitrary units). HD30614: V=4.3, 615sec. HD21428: V=4.7, 165sec, HD20041: V=5.8, 165sec, HD30034: V=5.4, 165sec, HD55730: V=5.7, 165sec, HD27971: V=5.7, 165sec, HD42471: V=5.8, 115sec.

Galaxy spectra

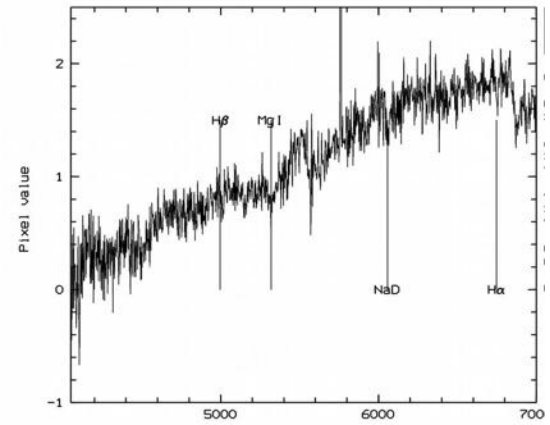

UGC 12127, 2700sec, V=15

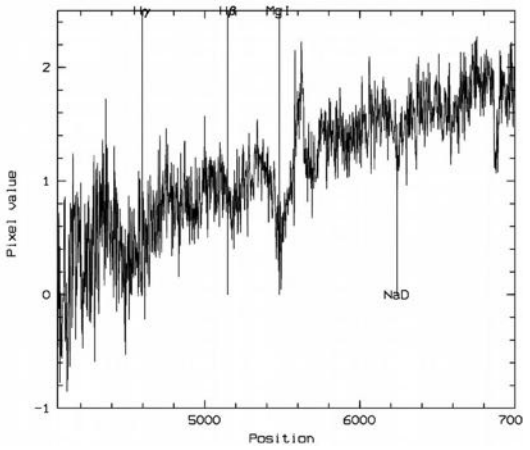

Xclass 102 BCG, 2700sec, V=15.1

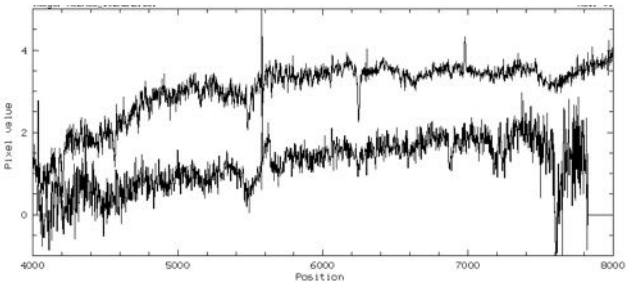

Xclass 102 BCG (MISTRAL 2700sec) + SDSS

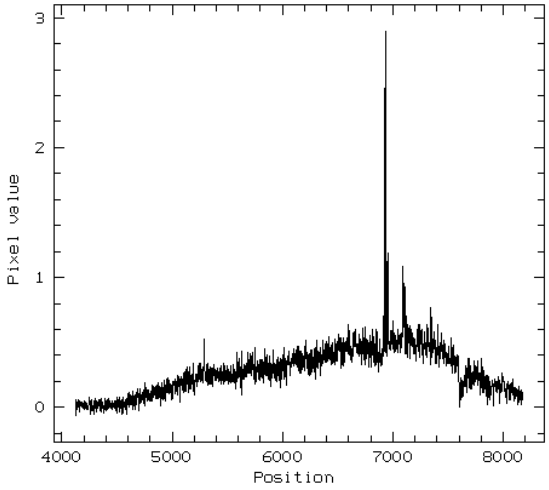

WISEA J025857.96+095748.3 , exp. Time : 7200sec, V=16.5

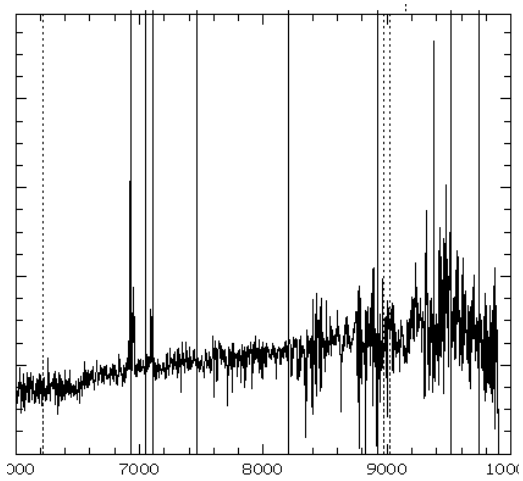

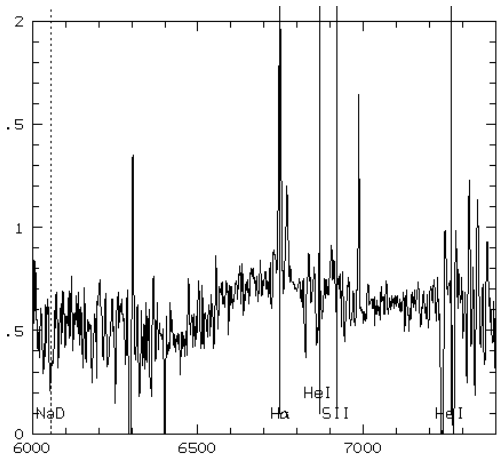

Host galaxy of at2020aaue, exp. Time : 3600sec	CGCG 064-083, exp. Time : 3600sec, V=15, Halpha flux : 113.5934 10^{-17} ergs/cm^2/s (SDSS)
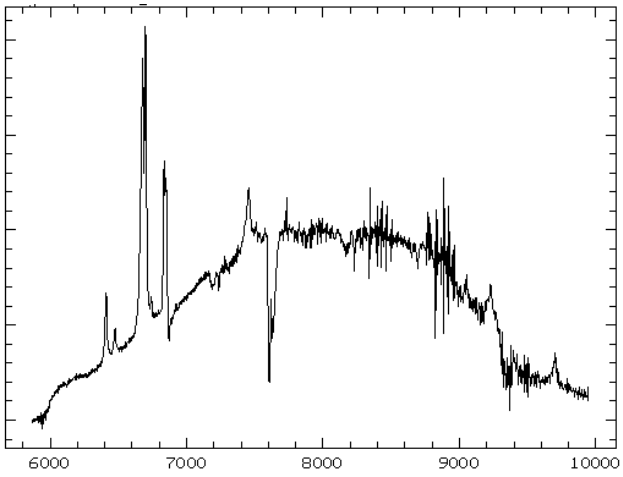	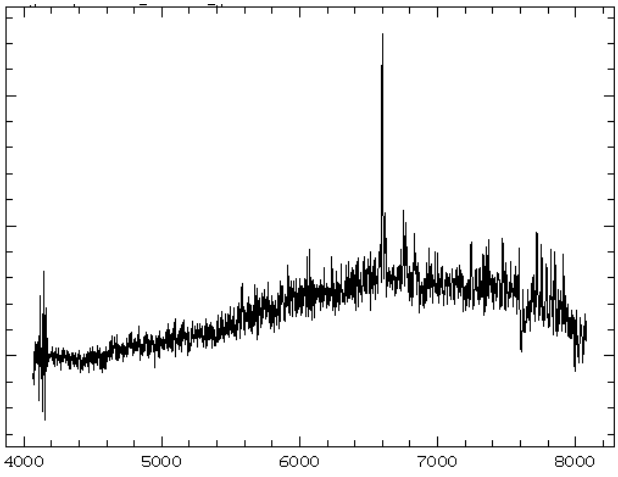
NGC1275, exp. Time : 1200sec, V=11.9, Halpha flux : 9.77E+09 Jy-Hz (NED)	NGC4330, exp. Time : 3600sec, V=12.5, Halpha flux : 124.3007 10^{-17} ergs/cm^2/s (SDSS)
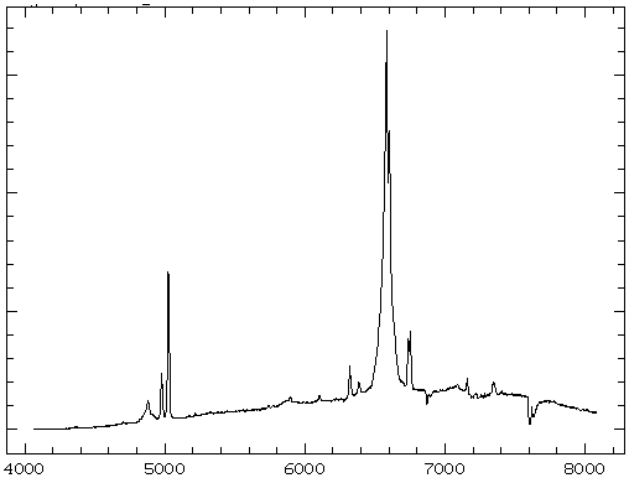	
NGC4151, exp. Time : 660sec, V=10.8, Halpha flux : 1.41E+12 Jy-Hz (NED)	
Figure A17 : Galaxies. Magnitudes are integrated values, not values inside the slit.	

Transient spectra

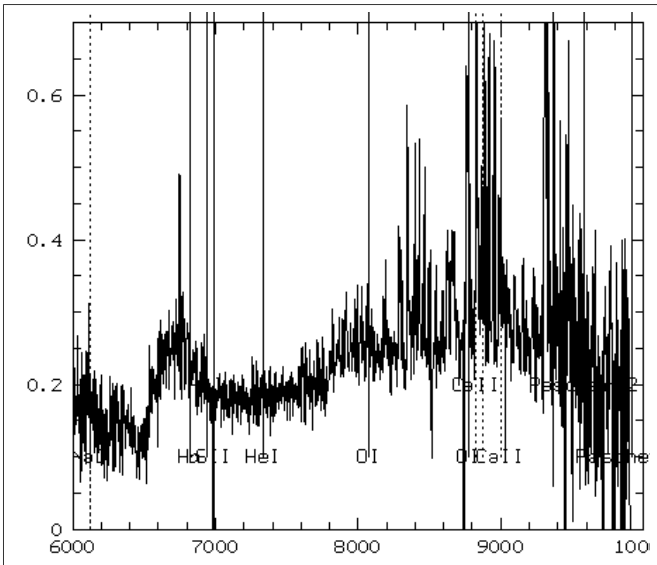

Gaia20fpd, SN, exp. Time : 3600sec, V=18.2

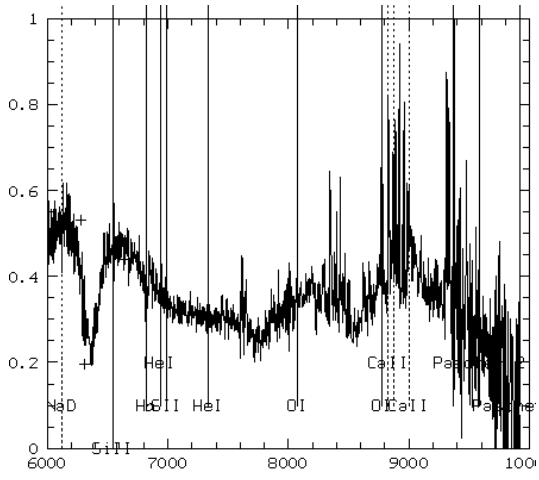

Gaia20fnu, SN, Exp. Time : 3600sec, V=17.7

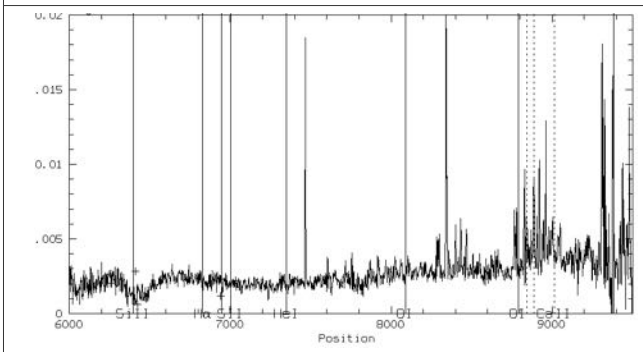

At2020abqq, SN, exp Time : 2400sec, V=18.6

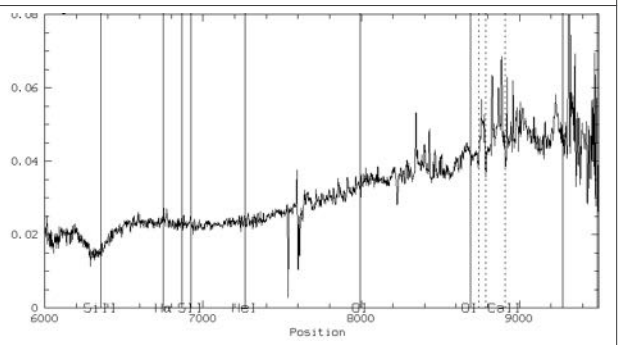

At2020abfa, SN, exp. Time : 3600 sec, V=18.6

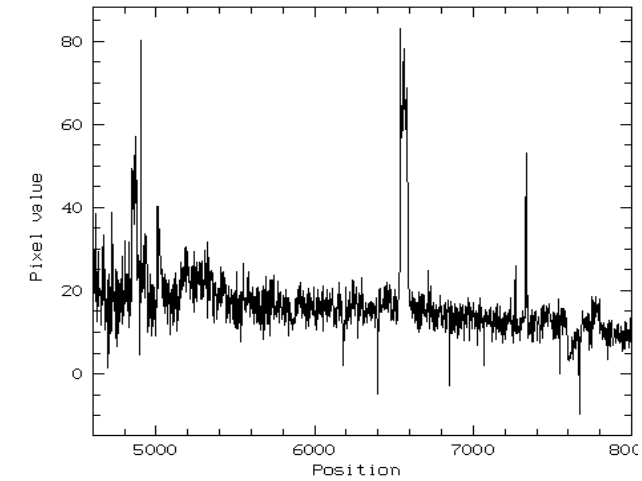

Nova in M31 (at2020aafw), exp. Time : 3600sec, V=18.5

Figure A18 : Transients

Galactic Nebulae spectra

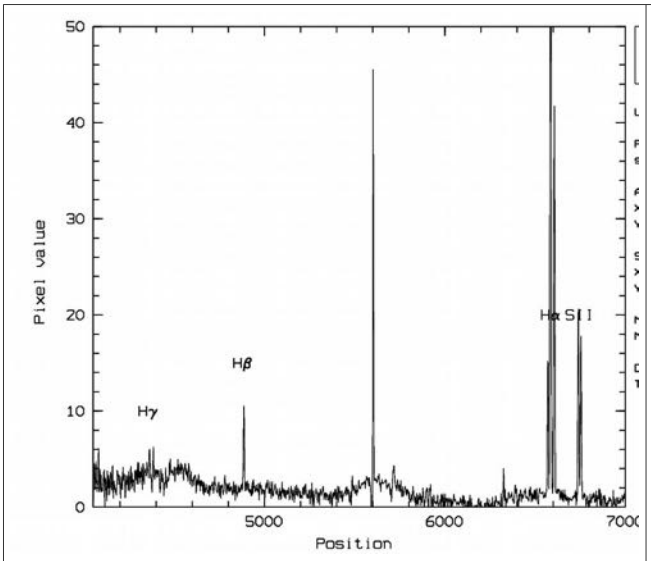

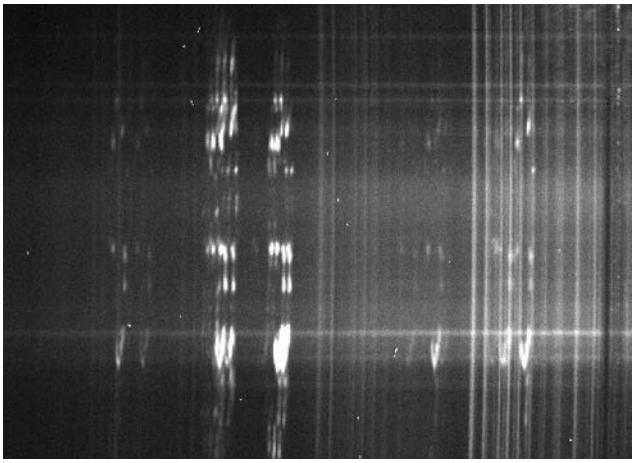

Sh2_252A nebula, 600sec	2D spectra of M1

Fig. A19: galactic nebulae : left : HII region, right : supernova remnant

Appendix X : MISTRAL fits header keywords

TableB4: MISTRAL fits header keywords and their meaning. Red underlined keywords are not correctly filled for now, they do not have then to be taken into account.	
BITPIX	int
NAXIS	number of axes
NAXIS1	
NAXIS2	
BSCALE	physical = BZERO + BSCALE*array_value
BZERO	physical = BZERO + BSCALE*array_value
DATE-OBS	YYYY-MM-DDThh:mm:ss observation, UT
EXPTIME	Exposure time in seconds
EXPOSURE	Exposure time in seconds
SET-TEMP	CCD temperature setpoint in C
CCD-TEMP	CCD temperature at start of exposure in C
XPIXSZ	Pixel Width in microns (after binning)
YPIXSZ	Pixel Height in microns (after binning)
XBINNING	Binning factor in width
YBINNING	Binning factor in height
XORGSUBF	Subframe X position in binned pixels
YORGSUBF	Subframe Y position in binned pixels
READOUTM	Readout mode of image
FILTER	Filter used when taking image
IMAGETYP	Type of image
FOCALLEN	Focal length of telescope in mm
APTDIA	Aperture diameter of telescope in mm
APTAREA	Aperture area of telescope in mm^2
SBSTDVER	Version of SBFITSEXT standard in effect
GAIN	Reading gain
SWCREATE	Name of CC software
SWSERIAL	Software serial number
SITELAT	Latitude of the observatory
SITELONG	Longitude of the observatory
JD	Julian Date at time of exposure
JD-HELIO	Heliocentric Julian Date at time of exposure
OBJECT	Target name

TELESCOP	Telescope used to acquire this image
INSTRUME	Instrument used to acquire this image
OBSERVER	Observer's name
NOTES	Additionnal notes
ROWORDER	Image write order, BOTTOM-UP or TOP-DOWN
FLIPSTAT	
RA	RA position of telescope
DEC	DEC position of telescope
EQUINOX	/equinox year for positions in this header
RADECSYS	e.g. FK5
ANGLE	Telescope rotator angle
AIRMASS	Relative optical path length through atmosphere
LST	
UTC	
MJD-OBS	
ORIGIN	Name of observatory
OBJ_ALRT	Alert (YES) or Regular (NO)
ARCHFILE	File name in the archive
CRVAL1	CTYPE1 coordinate of reference point
CRPIX1	pixel number (1 up) of reference point, axis 1
CTYPE1	e.g. RA---TAN
CRVAL2	CTYPE2 coordinate of reference point
CRPIX2	pixel number (1 up) of reference point, axis 2
CTYPE2	e.g. DEC--TAN
CDELT1	axis 1 pixel size in CTYPE1 units
CDELT2	axis 2 pixel size in CTYPE2 units
MOON_ILL	Moon Illumination in %
MOON_DIS	Object-Moon distance in degrees
CCDSHUTR	Shutter mode
CCDRON	CCD read out noise
CCDEGAIN	CCD gain
PIX_SKY	Pixel size in arcsec
LAMPFLAT	Spectral flat field lamp status : ON/OFF
LAMPARC	Spectral wavelength calibration lamp status : ON/OFF
MIR_CALI	Calibration mirror status : ON/OFF

SLIT	Slit status : ON/OFF
SLITWIDT	Slit aperture
SLITPOS	Slit position on the carriage
GRISM	Spectral dispersor status : BLUE/RED/NONE
GRISMPOS	Dispersor position on the carriage
OFS_SPEC	
LENSTYP	Instrument entrance lens (RED/BLUE)
MIST_FOC	MISTRAL focus position
SLITPIX	Slit position in x on the image (pixels)
YSHIFT	Grism y-shift (pixels)
MIST_TMP	MISTRAL instrument temperature
MIST_HYG	MISTRAL instrument hygrometry
SEEING	Measured seeing
TEMP_SKY	
RA_MEAN	
RA_RMS	
DEC_MEAN	
DEC_RMS	
FOCUS_TE	Telescope focus position
SWOWNER	Licensed owner of software

Appendix XI : quicklook.py

We give here the Python commands and the procedure used with quicklook.py (tested under python3.6, 3.7 and 3.8). This version has to launched from a control command window with an instruction like:

python3.6 quicklook.py λ_{min} λ_{max} level row a b c

```
# package import
import sys
import numpy as np
from aspired import image_reduction
from aspired import spectral_reduction
from astropy.io import fits
import plotly.io as pio
pio.renderers.default = "firefox"
from scipy import interpolate
import math
import os

# input parameters
minw = sys.argv[1]
minw = np.float(minw)
maxw = sys.argv[2]
maxw = np.float(maxw)
back = sys.argv[3]
back = np.float(back)
back = int(back)
xmean = sys.argv[4]
xmean = np.float(xmean)
xmean = int(xmean)
width = sys.argv[5]
width = np.float(width)
width = int(width)
skyw = sys.argv[6]
skyw = np.float(skyw)
skyw = int(skyw)
skys = sys.argv[7]
skys = np.float(skys)
skys = int(skys)


#pre reduction
science_frame                                                                    =
image_reduction.ImageReduction('/data/MISTRAL/softreduc/data/testNGC4330.txt',
exptime_dark=15., log_level='INFO', log_file_name=None)
science_frame.reduce()


# spectral reduction
```

```
science_frame_twodspec = spectral_reduction.TwoDSpec(science_frame, cosmicray=True, cosmicray_sigma = 5., log_file_name=None, gain=4.0)

# definition of place to extract spectrum
trace = np.arange(2045)
trace[:] = xmean
trace_sigma = np.arange(2045)
trace_sigma[:] = 1

 # extraction from 2D
science_frame_twodspec.add_trace(trace, trace_sigma)
science_frame_twodspec.ap_extract(apwidth=width, skysep=skys, skywidth=skyw, optimal=False, display=True)

science_frame_twodspec.extract_arc_spec(display=True)


#1D generation
reduction_onedspec = spectral_reduction.OneDSpec(log_file_name=None)
reduction_onedspec.from_twodspec(science_frame_twodspec, stype='science')


# wavelength calibration steps
reduction_onedspec.find_arc_lines(display=True,background=back,stype='science')

reduction_onedspec.initialise_calibrator(stype='science')

reduction_onedspec.set_hough_properties(num_slopes=1000,xbins=100,ybins=100,min_wavelength=minw,max_wavelength=maxw,stype='science')
reduction_onedspec.set_ransac_properties(filter_close=True,stype='science',linear='True')

# definition of MISTRAL calibration line sample
toto = ["2536", "2967", "3021", "3131", "3341", "3650", "4046", "4077", "4358", "4521", "4624", "4668", "4690", "4698", "4734", "4792", "4807", "4829", "4843", "4916", "4923", "5460", "5769", "5790", "6965", "7067", "7147", "7272", "7339", "7384", "7386", "7393", "7400", "7503", "7559", "7584", "7635", "7643", "7723", "7802", "7881", "7948", "7967", "8057", "8061", "8115", "8231", "8264", "8266", "8424", "8521", "8668", "8819", "9045", "9123", "9162", "9225", "9799", "9923", "10838"]

list = [2536.5, 2967.3, 3021.5, 3131.6, 3341.5, 3650.2, 4046.6, 4077.8, 4358.3, 4521.86, 4624.2, 4668.49, 4690.97, 4698.04, 4734.15, 4792.62, 4807.02, 4829.71, 4843.29, 4916.51, 4923.15, 5460.7, 5769.6, 5790.7, 6965.4, 7067.2, 7147.0, 7272.9, 7339.30, 7384.0, 7386.00, 7393.79, 7400.40, 7503.9, 7559.79, 7584.68, 7635.1, 7643.91, 7723.8, 7802.65, 7881.32, 7948.2, 7967.34, 8057.26, 8061.34, 8115.3, 8231.63, 8264.5, 8266.52, 8424.7, 8521.4, 8668.0, 8819.41, 9045.45, 9123.0, 9162.65, 9225.0, 9799.70, 9923.19, 10838.37]

reduction_onedspec.load_user_atlas(elements=toto,wavelengths=list)

reduction_onedspec.do_hough_transform(stype='science')
reduction_onedspec.fit(max_tries=100, stype='science')
```

```
reduction_onedspec.apply_wavelength_calibration(stype='science')


# take into account local extinction curve
extinction_table = fits.open('/data/MISTRAL/softreduc/OHPMinstral-main/20210122/data/extiohp.fits')[1].data
ohp_extinction = interpolate.interp1d(extinction_table['wave'], extinction_table['exti_ohp'], fill_value='extrapolate')
reduction_onedspec.set_atmospheric_extinction(extinction_func=ohp_extinction)

reduction_onedspec.apply_atmospheric_extinction_correction()
reduction_onedspec.inspect_reduced_spectrum(stype='science',wave_min=minw,wave_max=maxw,save_png=True)

#generate usable fits file with counts in HDU1, uncertaintyi HDU2, and sky (wavelength) in HDU3
reduction_onedspec.save_fits(output='count_resampled',filename='reduced',stype='science',overwrite=True)

# remove nan values in spectrum and generate final spectrum: "reduced_science_0_withoutnan.fits"
hdul = fits.open('reduced_science_0.fits')
data = hdul[1].data
for index, value in enumerate(data):
    if  math.isnan(value):
      data[index] = 0.

os.system("rm reduced_science_0_withoutnan.fits")
hdul.writeto('reduced_science_0_withoutnan.fits')
hdul.close()
```

Appendix XII : Spot diagrams and vigneting curves

Fig. A20 MISTRAL's image quality spot diagrams from 0.4 to 0.8 microns, along with predicted RMS for these five wavelengths.

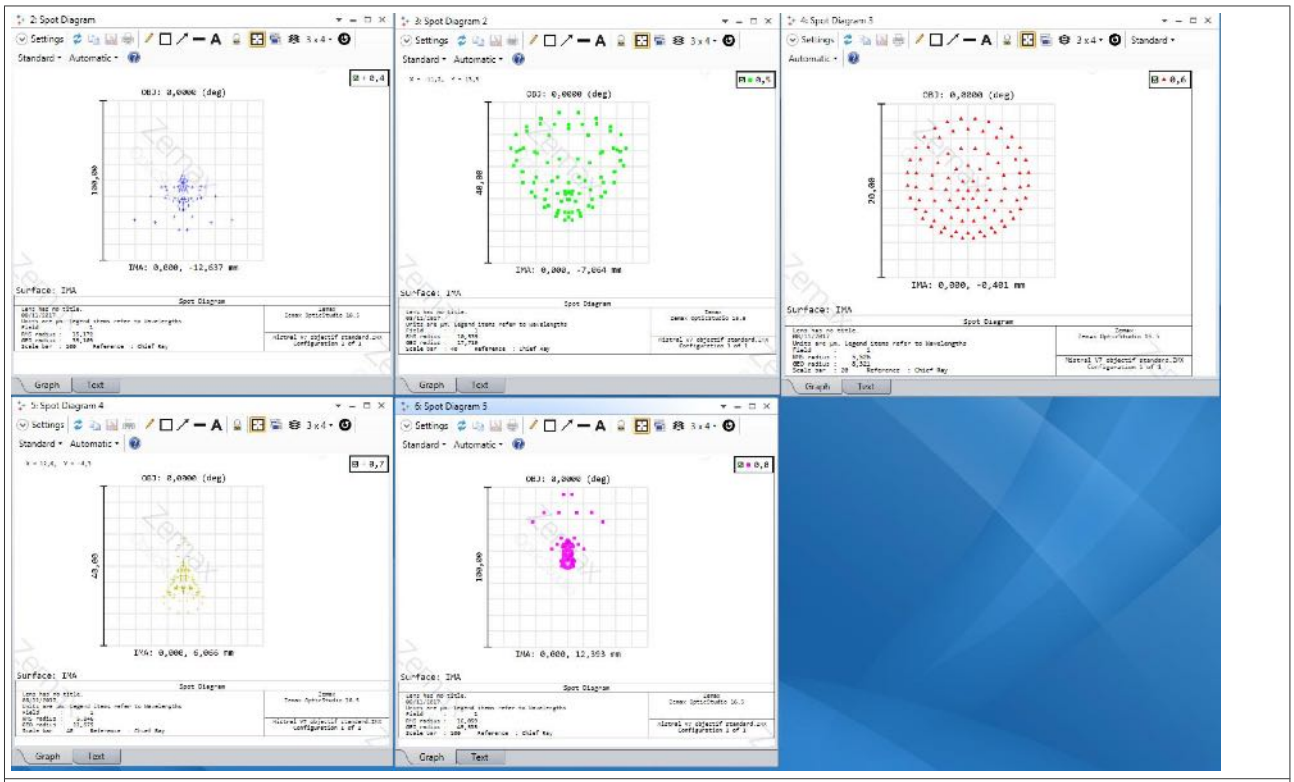

Fig. A20: image quality spot diagrams from 0.4 to 0.8 microns

Fig. A21 Vigneting curves versus field radius in degrees, at 400 and 800 nm, for the blue entrance lens of MISTRAL .

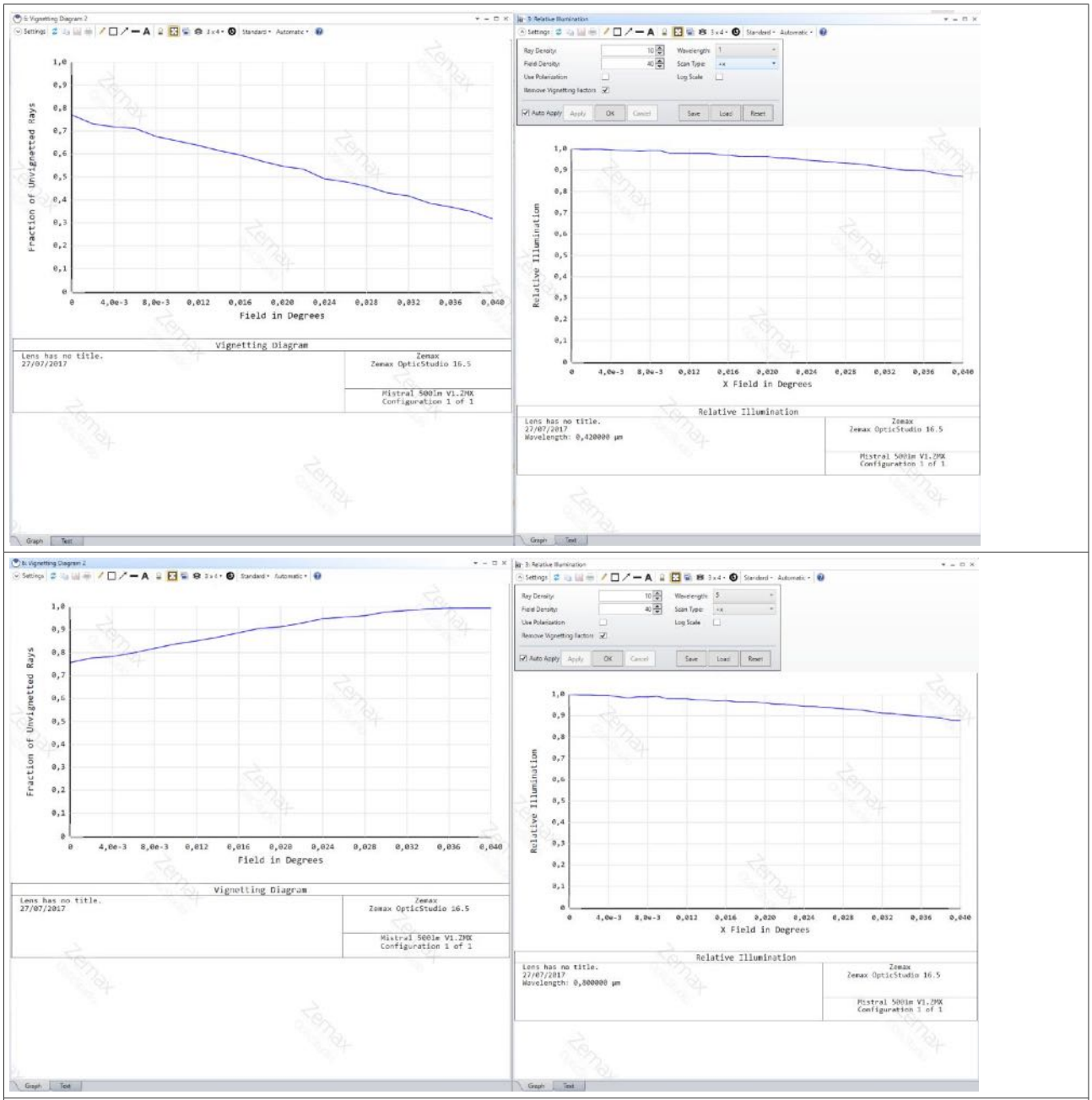

Fig. A21. Vigneting curves versus field radius in degrees, at 400 and 800 nm, for the blue entrance lens of MISTRAL . Upper part : 420 nm, lower part 800nm

Appendix XIII : filter response curves

Table B5 gives the main filter characteristics.

Name	Origin	Central λ	Max trans.	50 % low	50 % high
SDSS g’	Astrodon	~470nm	>99 %	401nm	549nm
SDSS r’	Astrodon	~630nm	>99 %	563nm	695nm
SDSS i’	Astrodon	~770nm	>99 %	694nm	847nm
SDSS z’	Astrodon	>840nm	>99 %	825nm	...
SDSS Y	Astrodon	>950nm	>92 %	950nm	...
Hβ 5nm		~486nm	>92 %	481nm	492nm
OIII 5 nm	Astrodon	~502nm	>98 %	499nm	504.1nm
Hα 3 nm	Astrodon	~656.5nm	>96 %	654.8nm	658nm
SII 5 nm	Astrodon	~671nm	>97 %	668.7nm	674nm
LongPass OD4 400 nm	Edmund	>400nm	>98 %	400nm	...
LongPass OD4 600 nm	Edmund	>600nm	>98 %	599.4nm	...
LongPass smooth 400 nm		>400nm	>90 %	400nm	...
LongPass smooth 600 nm		>600nm	>90 %	570.6nm	...

Table B5: Filter basic characteristics

Filters transmission curves

The MISTRAL filters transmission was measured with the LAM Perkin-Elmer spectrograph between 400 and 1000nm, using the PMT and InGaAs sources and low (4A) and high (2A) resolution. The Perkin-Elmer spectrograph configurations are given in Fig. A22.

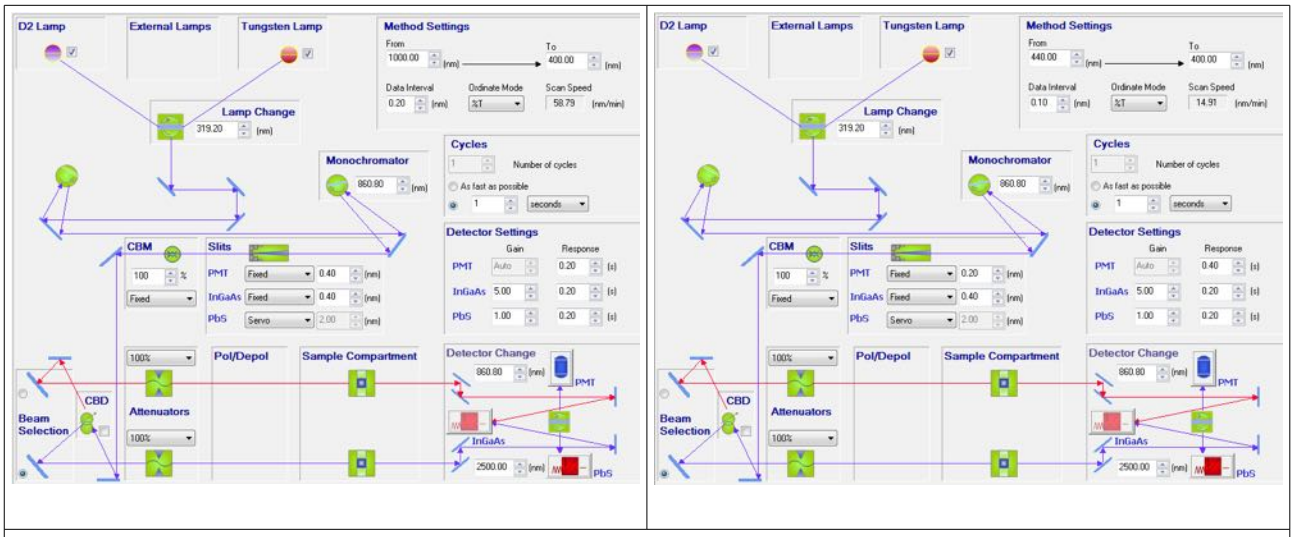

Fig. A22: Left : Perkin-Elmer low resolution configuration. Right : Perkin-Elmer high resolution configuration.

Fig A23 presents the passband of the 11 MISTRAL filters. The left column is a zoom on the useful

wavelength domain. The right column presents the filters transmission between 400 and 1000nm. The wide range filters (g', r', i', z', Y, passe-haut 400-1000nm, passe-haut 600-1000nm) were measured with a resolution of 4A (one measure point every 2A with a measured domain of 4A). The narrow-band filters (Hβ, OIII, Hα, SII) were measured with a resolution of 4A (one measure point every 2A with a measured domain of 4A) between 400 and 1000nm and with a resolution of 2A (one measure point every A with a measured domain of 2A) around their useful domain (right column). Ascii tables are available through the MISTRAL web page (http://www.obs-hp.fr/guide/mistral/MISTRAL_spectrograph_camera.shtml).

g', 0.4nm resolution	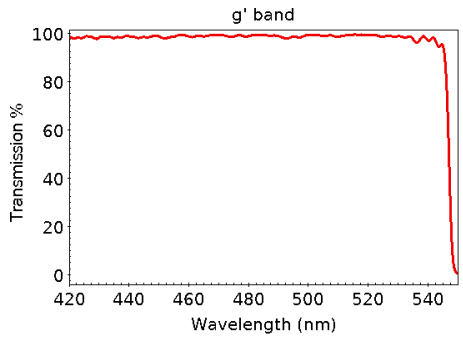	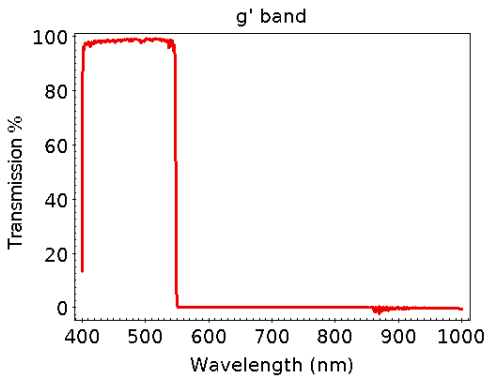
r', 0.4nm resolution	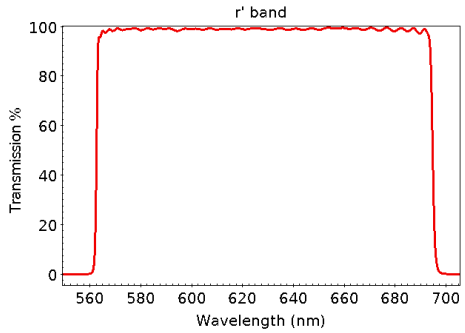	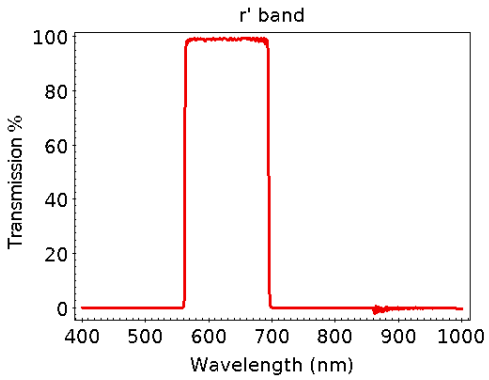
i', 0.4nm resolution	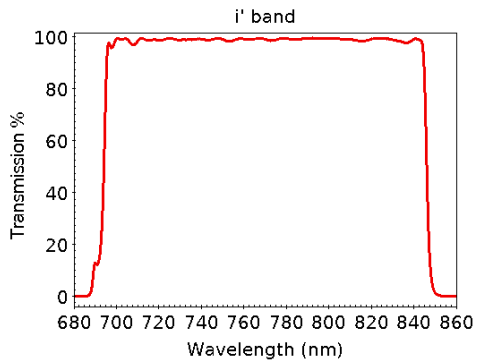	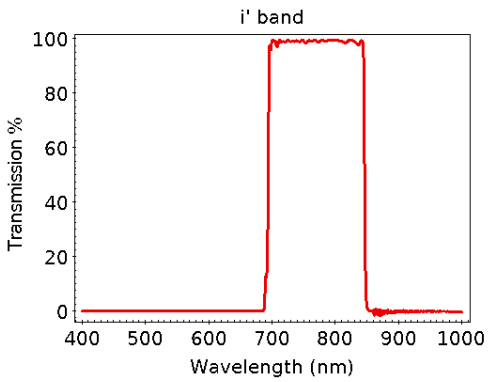

z', 0.4nm resolution	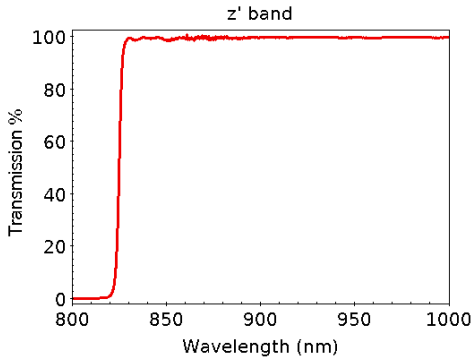	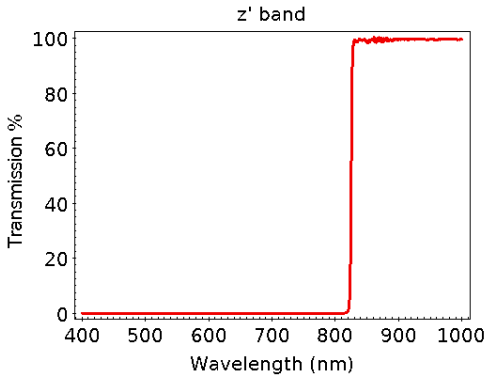
Y, 0.4nm resolution	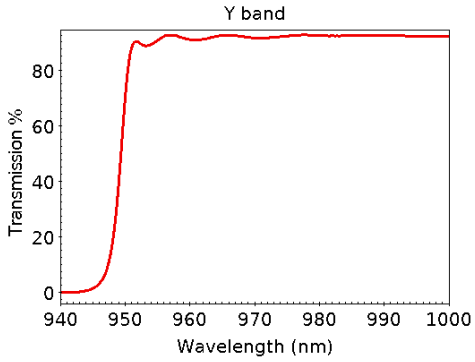	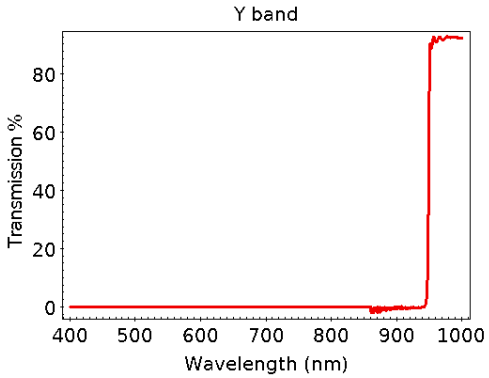
Hβ, left : 0.2nm resolution, right : 0.4nm resolution.	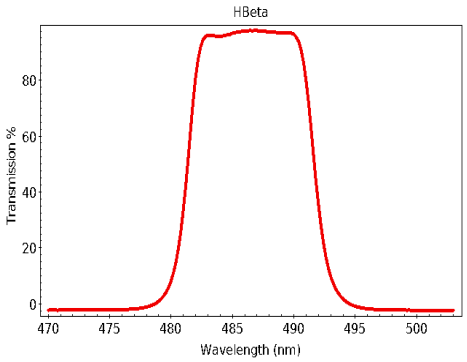	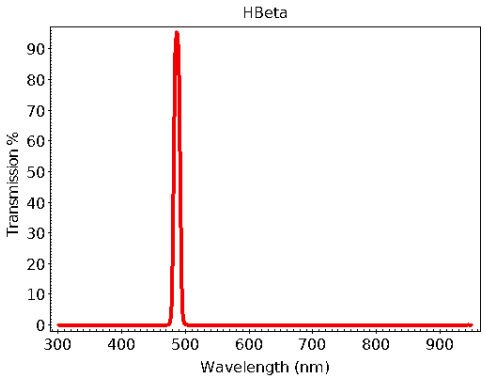
OIII, left : 0.2nm resolution, right : 0.4nm resolution	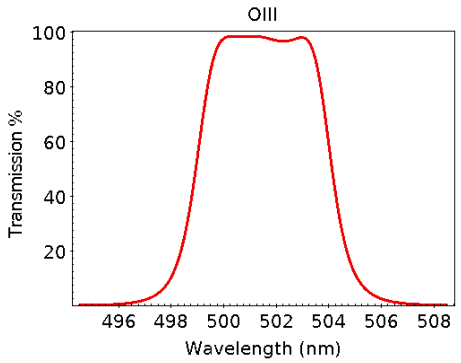	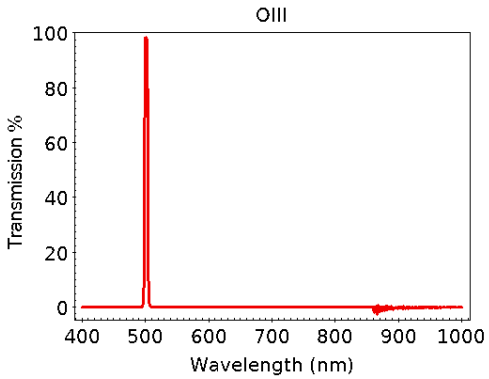

Hα, left : 0.2nm resolution, right : 0.4nm resolution	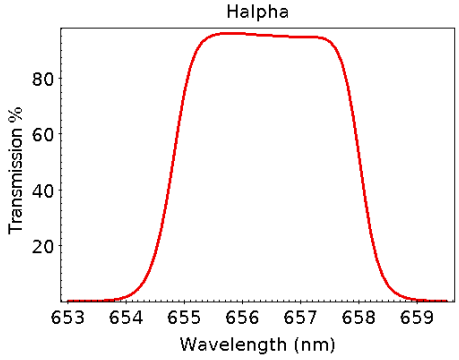	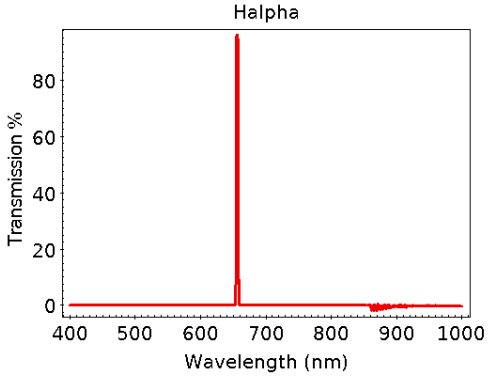
SII, left : 0.2nm resolution, right : 0.4nm resolution	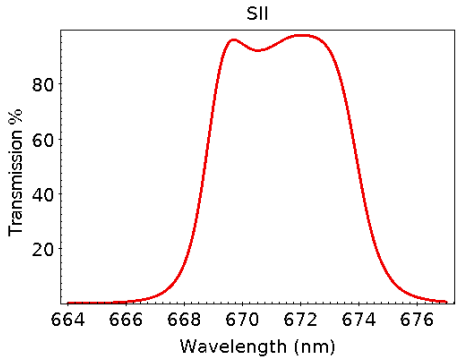	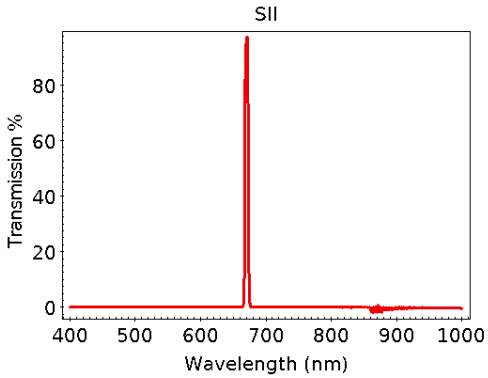
Blue order separation,left : 0.2nm resolution, right : 0.4nm resolution	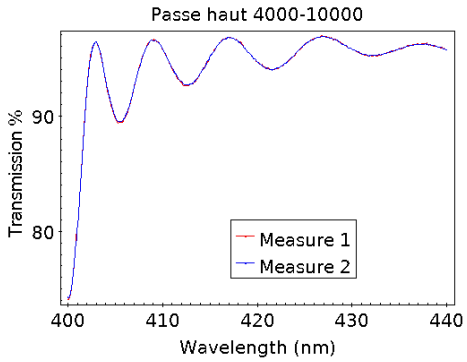	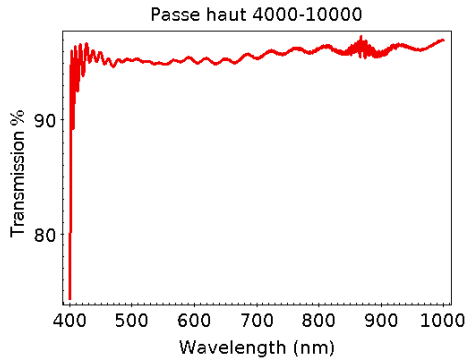
Red order separation,left : 0.2nm resolution, right : 0.4nm resolution	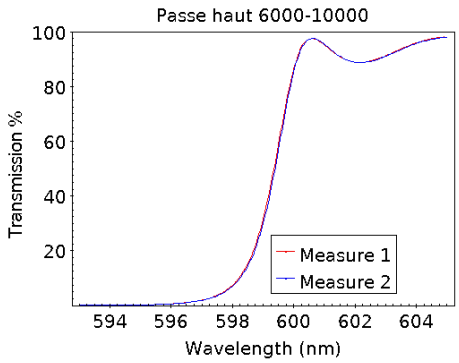	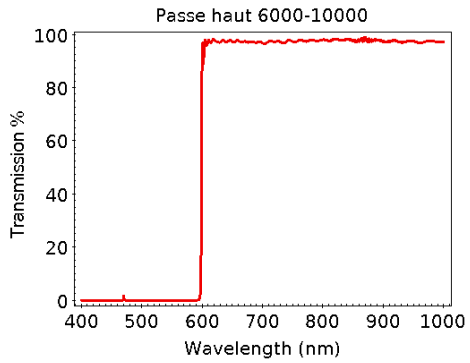

Smooth blue and red order separation, 0.4nm resolution.

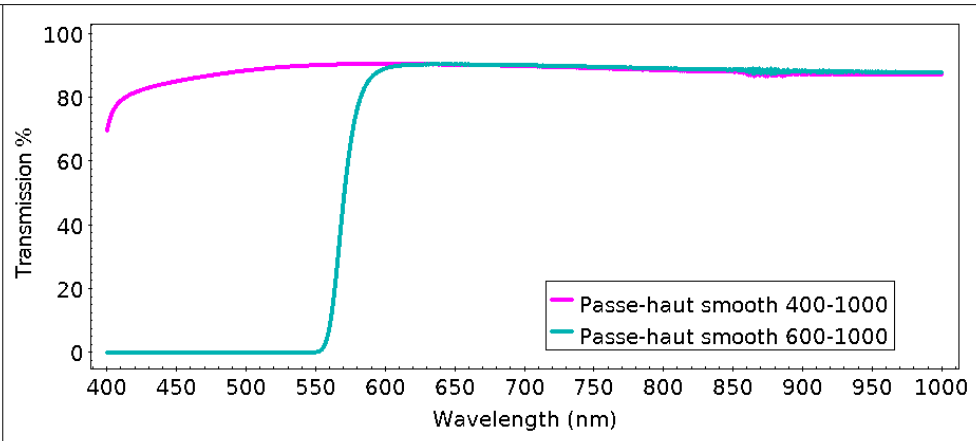

Fig. A23 : Passband of the MISTRAL filters.

Measure precision and uncertainties

Perkin-Elmer spectrograph switches between PMT and InGaAs

When reaching wavelengths of ~860nm, the spectrograph changes the monochromators' gratings (different grooves pitch and coatings for UV/Vis and NIR wavalengths) and switches between the photomultiplier and InGaAs detectors. This induces some additionnal noise in the transmission measures, at less than the 2 % level (see fig .A24), and roughly ~0.5 %. This means that above 860nm, one must add an additionnal uncertainty of less than 2 % to the transmission measures.

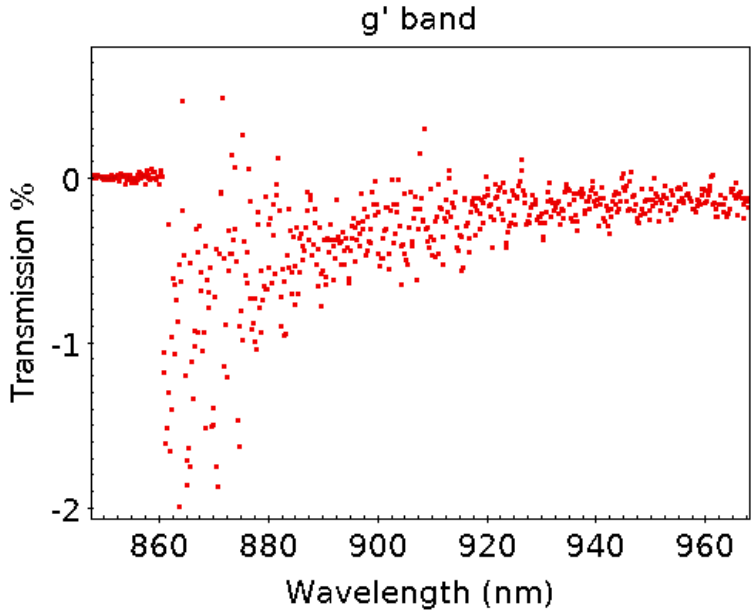

Fig. A24: zoom on the g' transmission curve close to the PMT/InGaAs switch.

Repetability between two consecutives measures

The differences in transmission percentage between two consecutive measures (without filter repositionning between two measures) were estimated in Fig. A25 with the SII filter measured at high resolution. The difference between the two measures is well below the 1 % level, and the shift in wavelength is lower than 0.01nm.

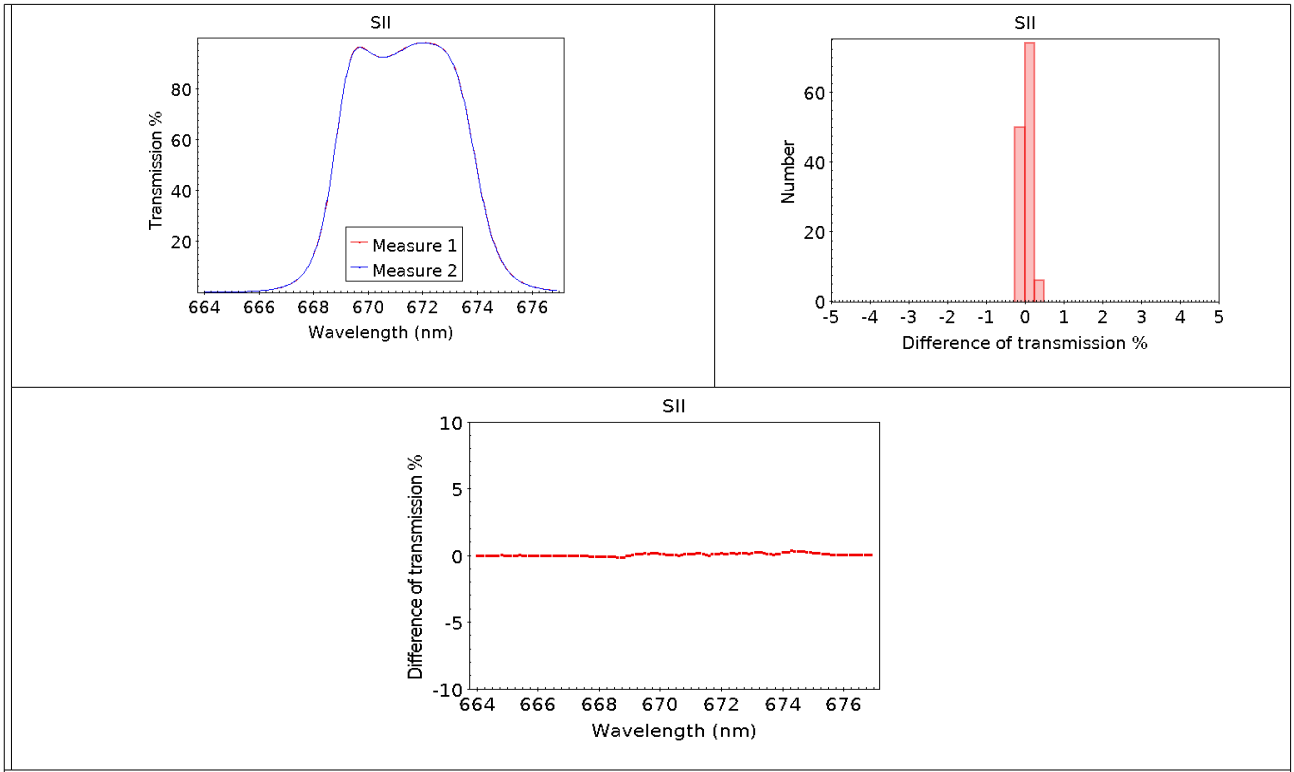

Fig. A25. Upper left : transmission curve ; upper right : histogram of the transmission percentage differences ; lower : transmission percentage differences versus wavelength.

Uncertainty due to residual angle between incident light and filter

When positionning the filter to measure, some non 90deg angle may be present between incident light and filter. This residual angle is most of the time of the order of 1deg or less. Fig. A26 estimates the effect of such an angle considering two measures (with filter repositionning between two measures) of the i' filter (low resolution) and of the OIII filter (high resolution). The difference between the two measures is well below the 2 % level (at the filter edges, where the wavelength shift is the largest), and the shift in wavelength is lower than 0.1nm.

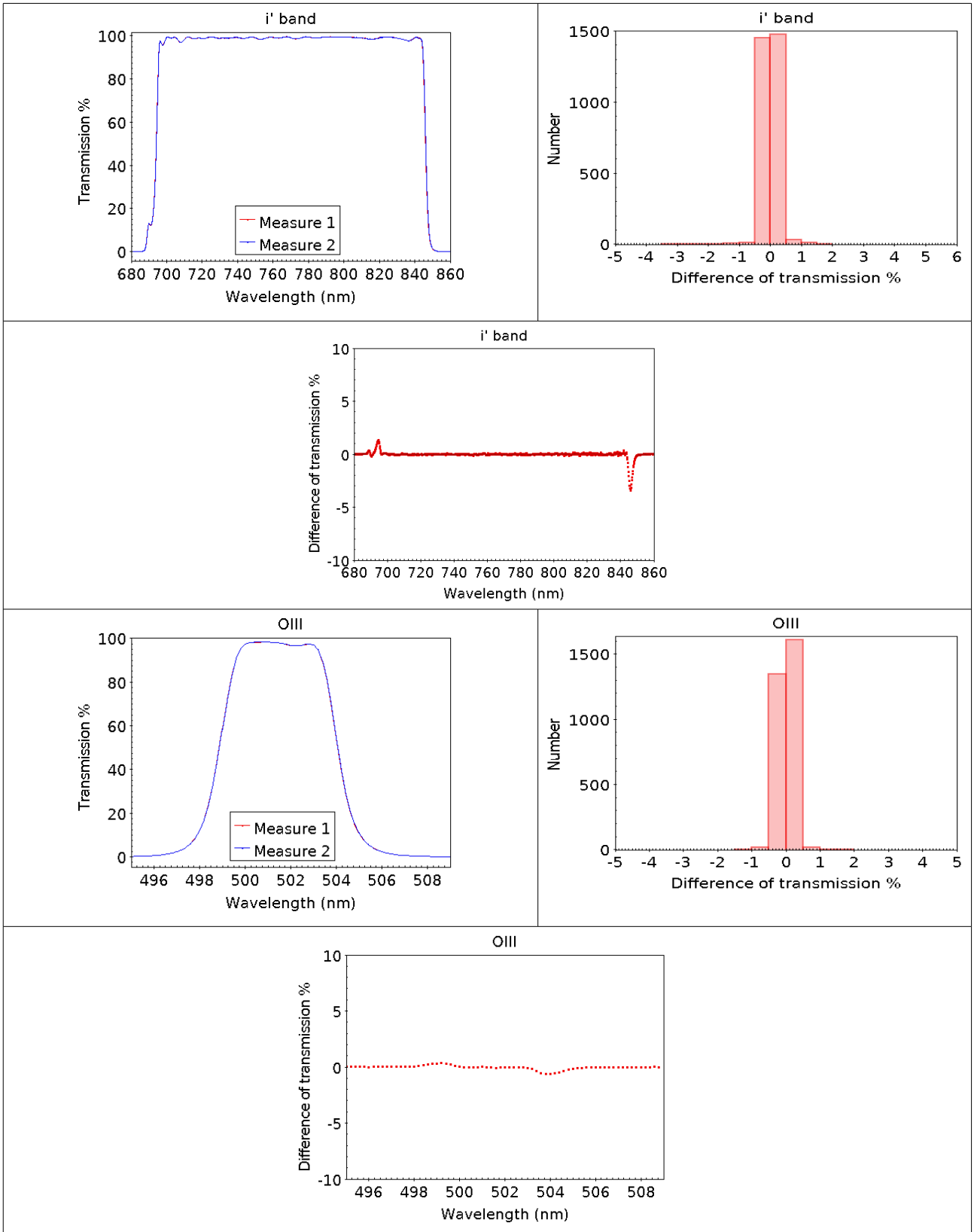

Fig. A26. For i' (measured at low resolution) and OIII (measured at high resolution) filters : Upper left : transmission curve ; upper right : histogram of the transmission percentage differences ; lower : transmission percentage differences versus wavelength.

Uncertainty due to residual angle between incident light and filter + filter side exchange

When positionning the filter to measure, in addition to some non 90deg angle between incident light and filter, the filter side toward the incident light can be exchanged. This can put in evidence some differences between the coating of the two filter sides. Fig. A27 estimates these effects considering two measures (with filter 180deg rotation between two measures) of the two passe-haut filters (side of the filters at high resolution), of the Hα filter (high resolution) and of the Hβ filter (high resolution). The difference between the two measures is less than the 2 % level (at the filter edges, where the wavelength shift is the largest), and the shift in wavelength is lower than 0.25nm, being most of the time of the order of 0.05nm.

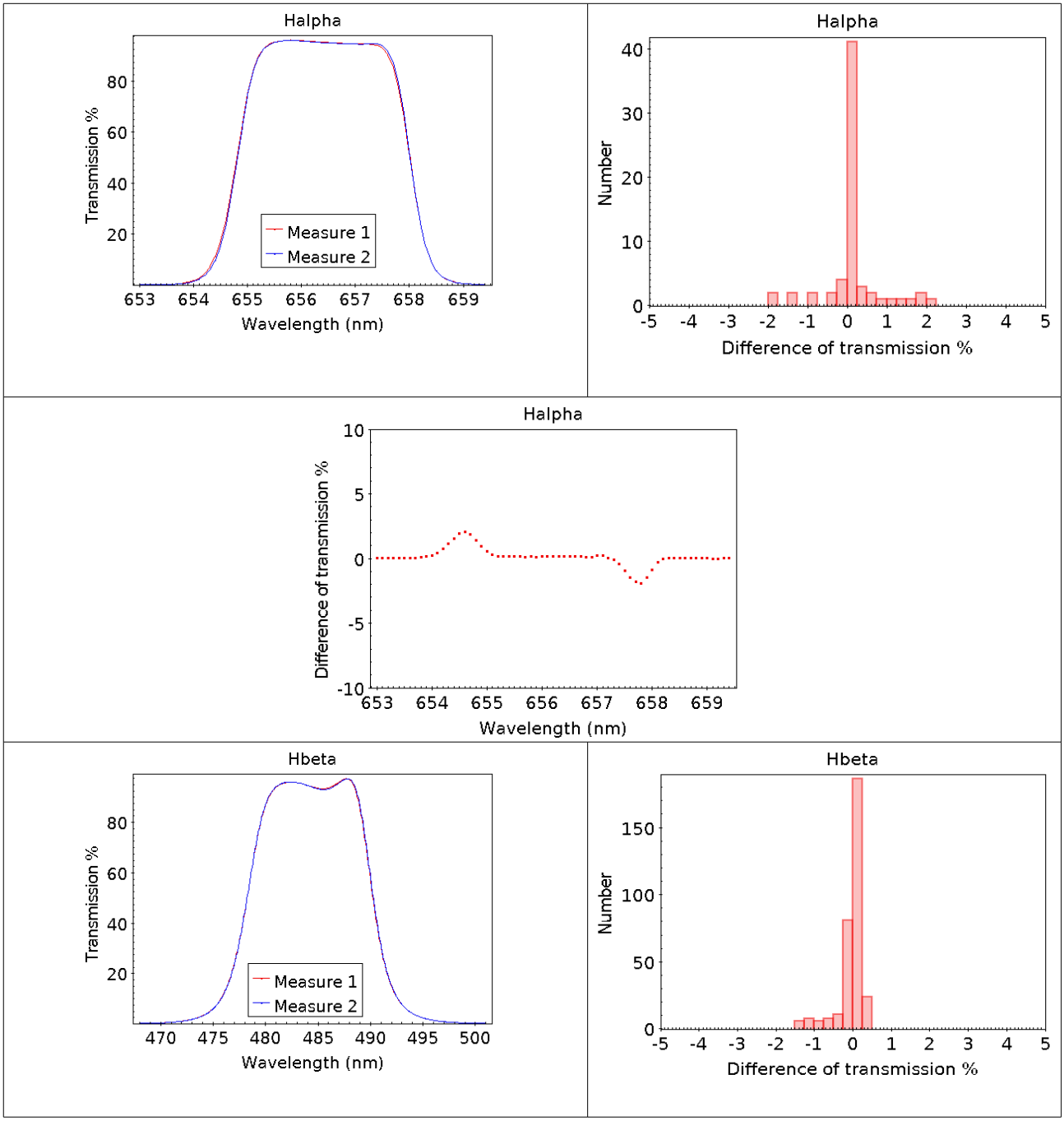

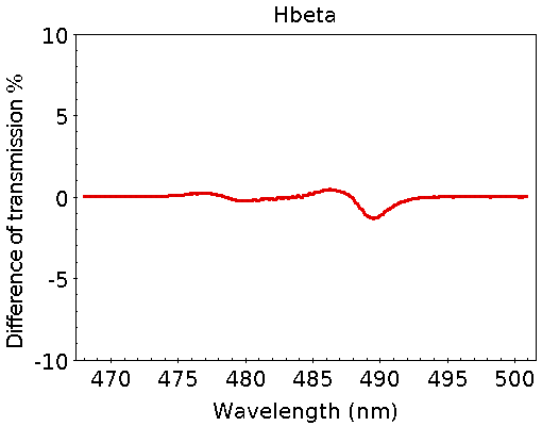
Hbeta
Difference of transmission %
10
5
0
-5
-10
470
475
480
485
490
495
500
Wavelength (nm)

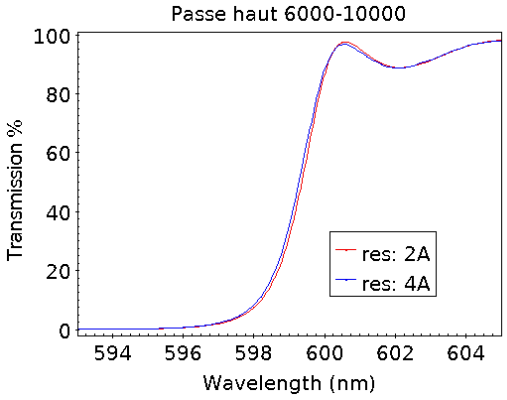
Passe haut 6000-10000
Transmission %
100
80
60
40
20
0
res: 2A
res: 4A
594
596
598
600
602
604
Wavelength (nm)

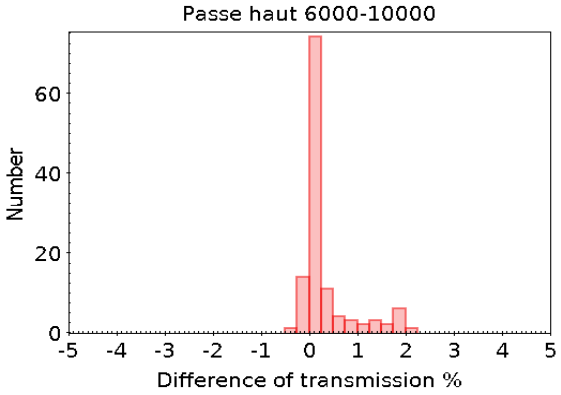
Passe haut 6000-10000
Number
60
40
20
0
-5
-4
-3
-2
-1
0
1
2
3
4
5
Difference of transmission %

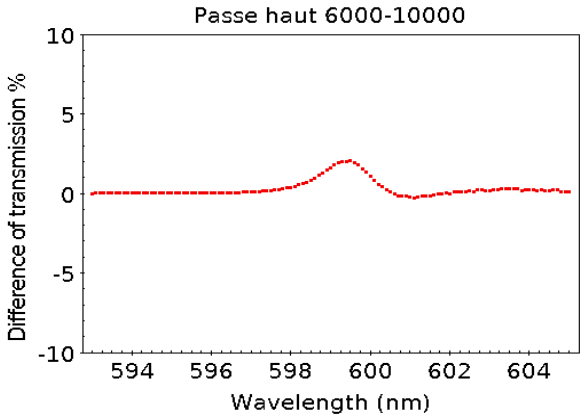
Passe haut 6000-10000
Difference of transmission %
10
5
0
-5
-10
594
596
598
600
602
604
Wavelength (nm)

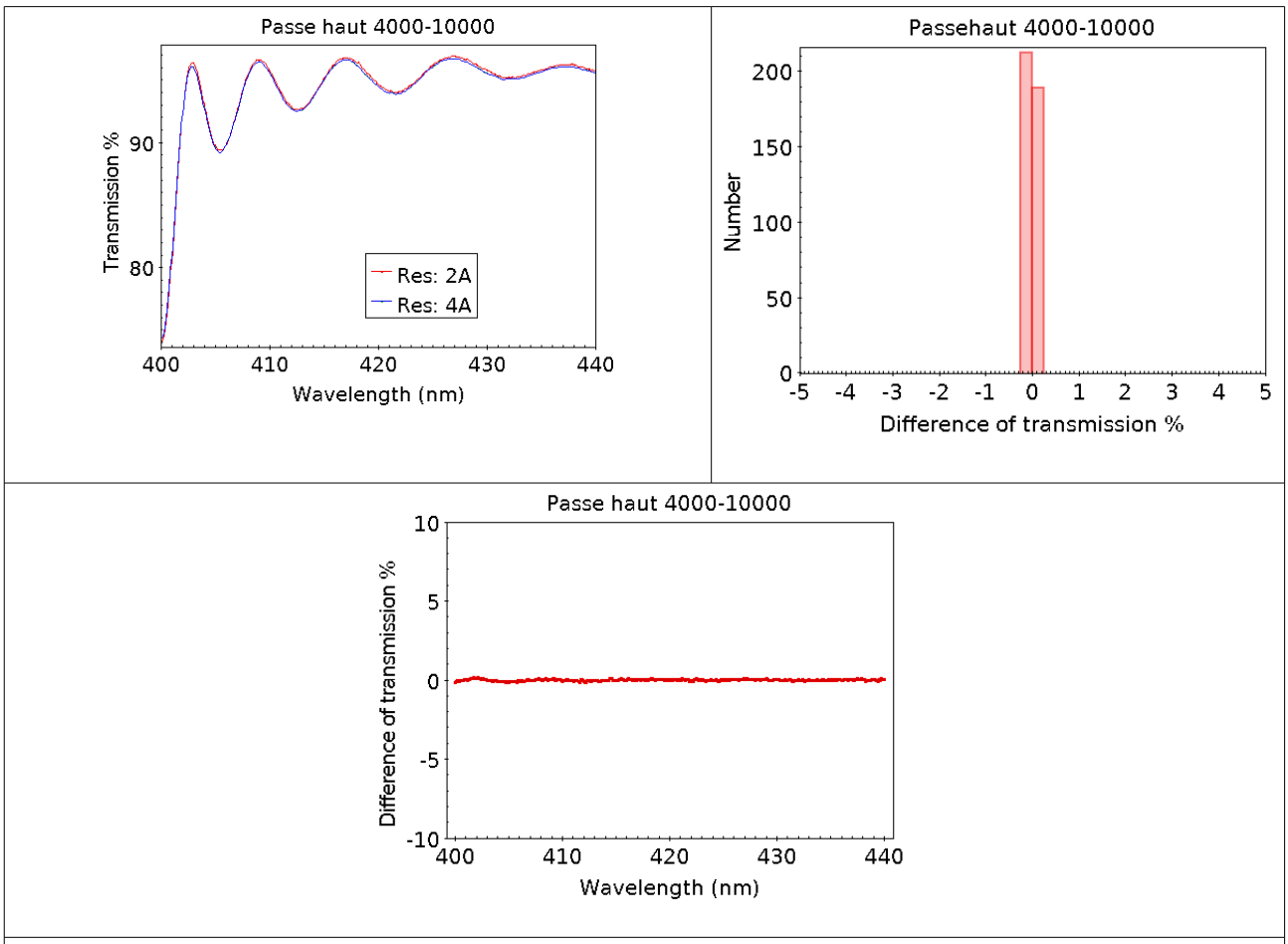

Fig. A27. For Hα, Hβ, Passe-haut 400-1000 and 600-1000 (all measured at high resolution) filters : Upper left : transmission curve ; upper right : histogram of the transmission percentage differences ; lower : transmission percentage differences versus wavelength.

Uncertainty due to angle of 5deg between incident light and filter

The effect of a 5deg angle positionning difference between two consecutive measures was estimated in Fig.A28. This was done at low resolution with the g', r', and i' filters. The difference between the two measures is less than the 10 % level at the filter edges, where the wavelength shift is the largest, and of the order of 2% in the middle of the response function. The shift in wavelength is lower than 1.6nm.

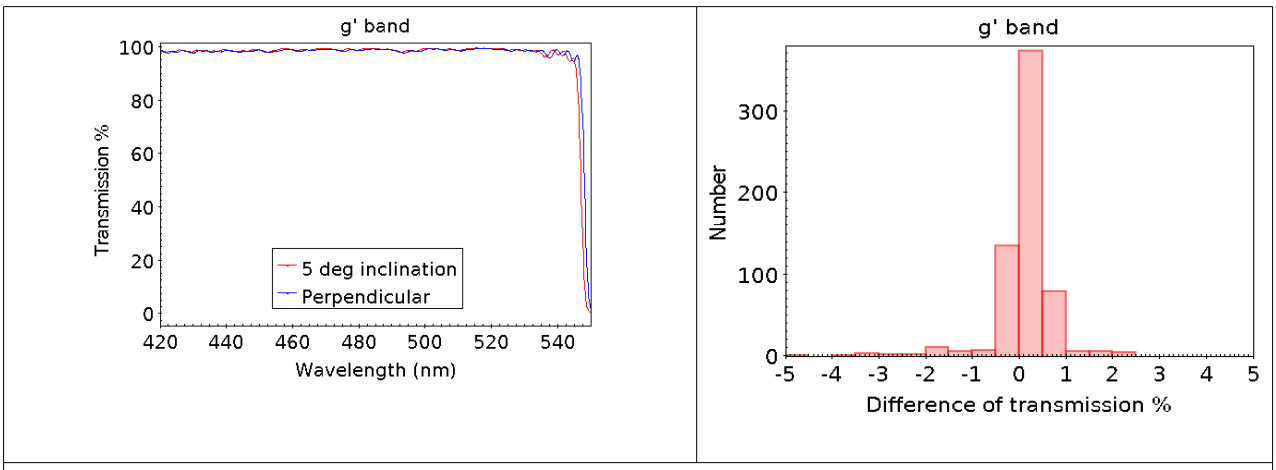
g' band
Transmission %
Wavelength (nm)
5 deg inclination
Perpendicular

g' band
Number
Difference of transmission %

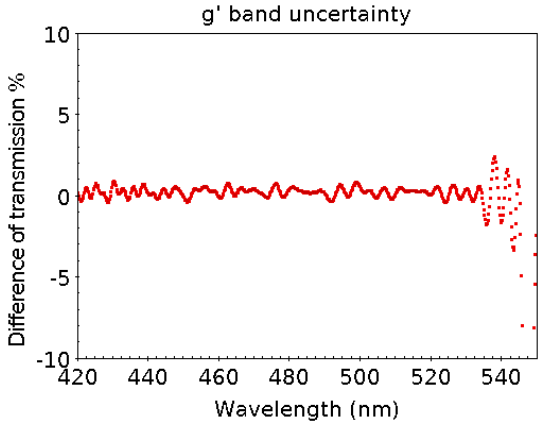
g' band uncertainty
Difference of transmission %
Wavelength (nm)

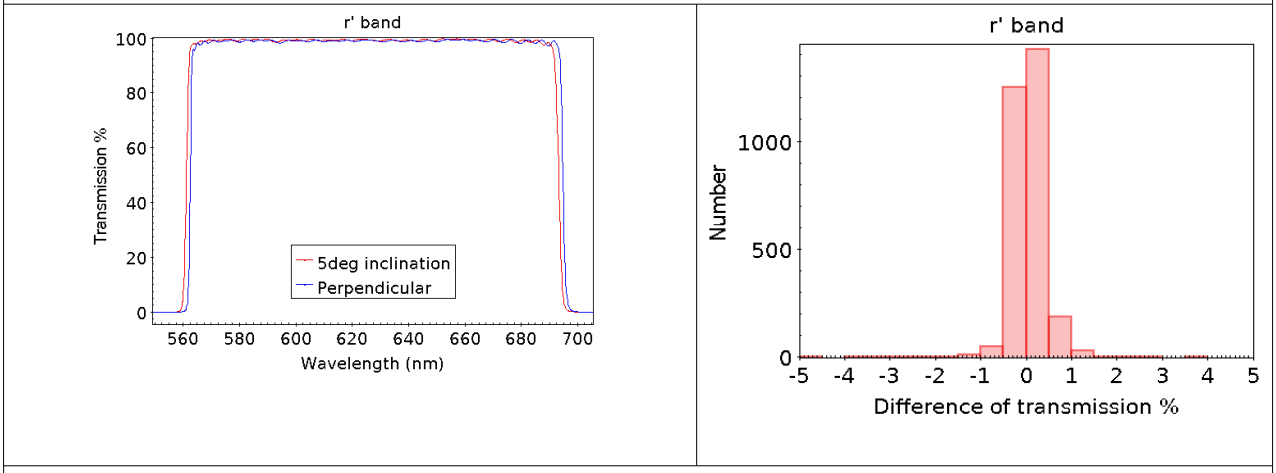
r' band
Transmission %
Wavelength (nm)
5deg inclination
Perpendicular

r' band
Number
Difference of transmission %

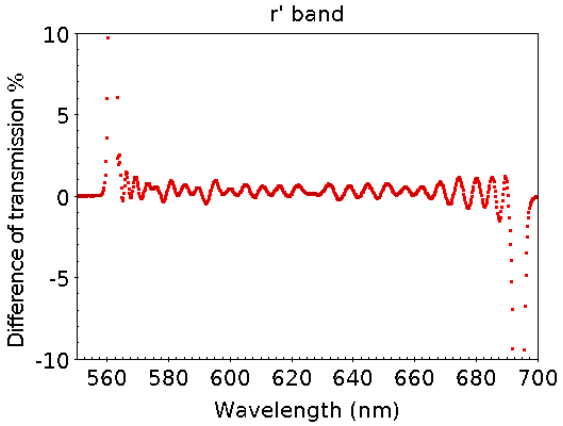
r' band
Difference of transmission %
Wavelength (nm)

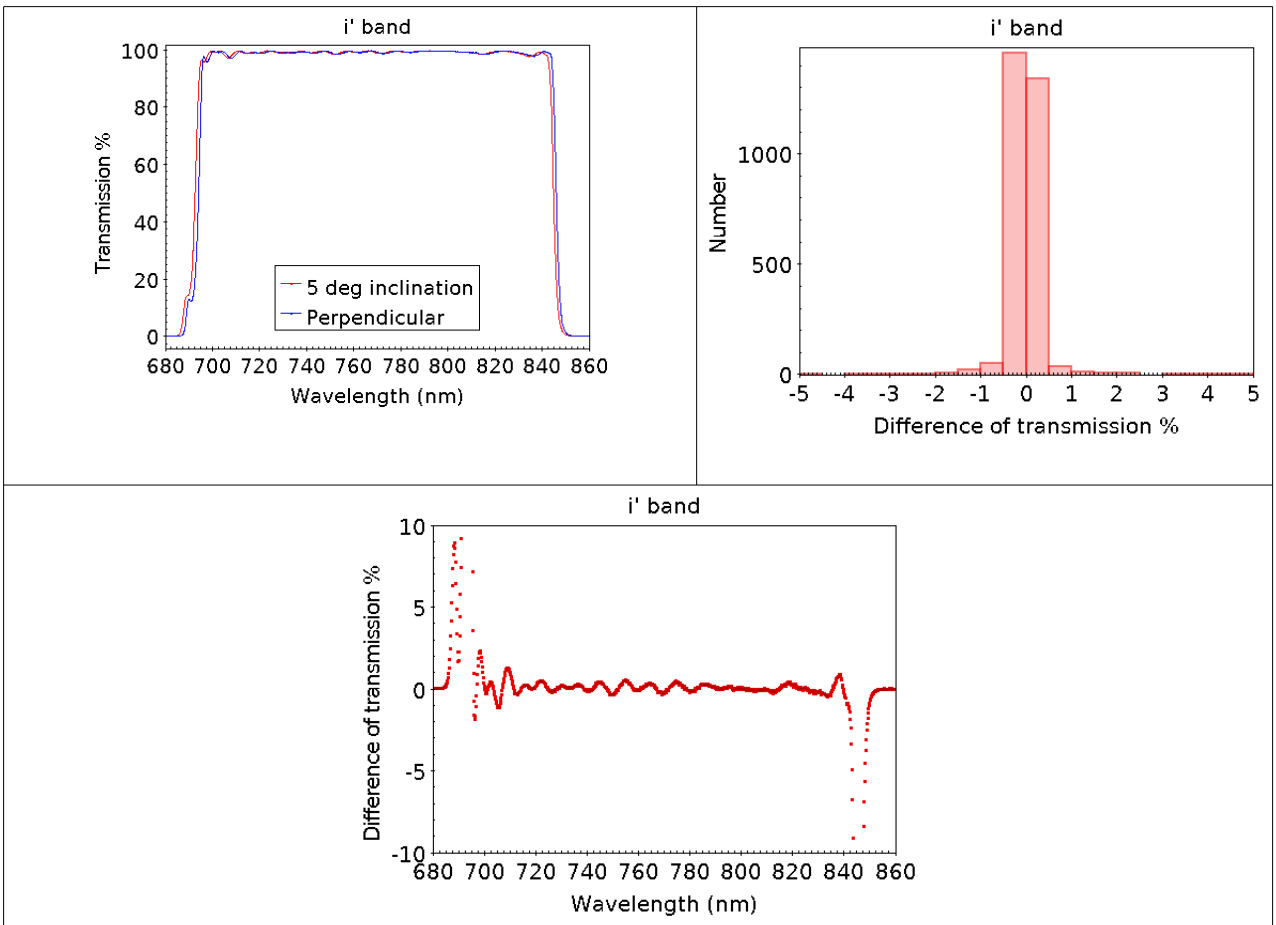

Fig. A28. For g', r', and i' (all measured at low resolution) filters : Upper left : transmission curve ; upper right : histogram of the transmission percentage differences ; lower : transmission percentage differences versus wavelength.

Uncertainty on the 100 % level

Before and after a filter measure, systematical checks of the 100 % level (internal calibration without filter on the optical path) were performed. Fig. A29 shows these 100 % level checks at low and high resolutions. The typical noise to add is below the 0.5 % level. The already described effect of the spectrograph switch between PMT and InGaAs sources at 860nm is well visible.

LR	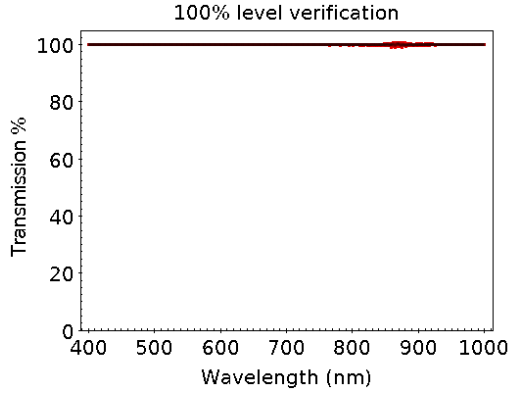	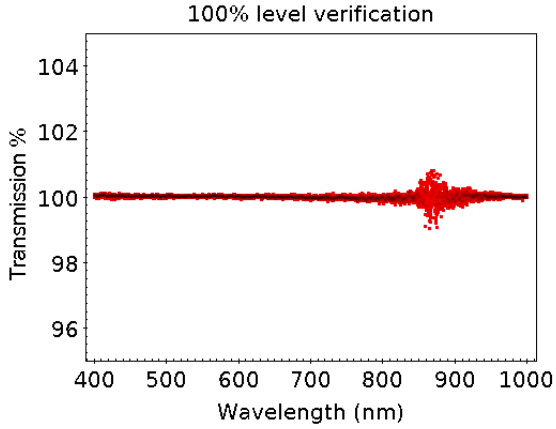
HR	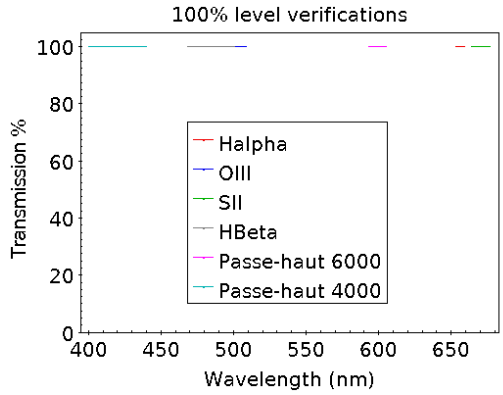	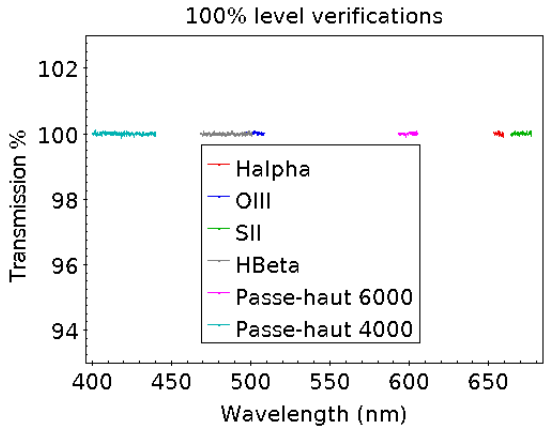
Fig. A29 : checks of the 100 % level		

Summary

Table B6 present the summary of the previously descrived uncertainty sources.

Table B6	Transmission induced difference	Wavelength shift
Intrinsic differences between two consecutive measures	<1 %	<0.01 nm
Residual incident angle between two consecutive measures with filter repositionning	<2 %	<0.1 nm
Residual incident angle between two consecutive measures with filter repositionning + side exchange	<2 %	<0.25nm
5deg between two consecutive measures	<10 % (edges of response function), <2 % (middle of response function)	<1.6nm
Internal 100 % level uncertainty	0.5 %	N/A

Appendix XIV : Guiding drifting curves

We give in Fig. A30 examples of individual drifting curves used to map the MISTRAL guiding drifts. Along alpha axis the ellapsed time is shown (in seconds) and along the y axis the drifting amplitude is shown (in arcsec).

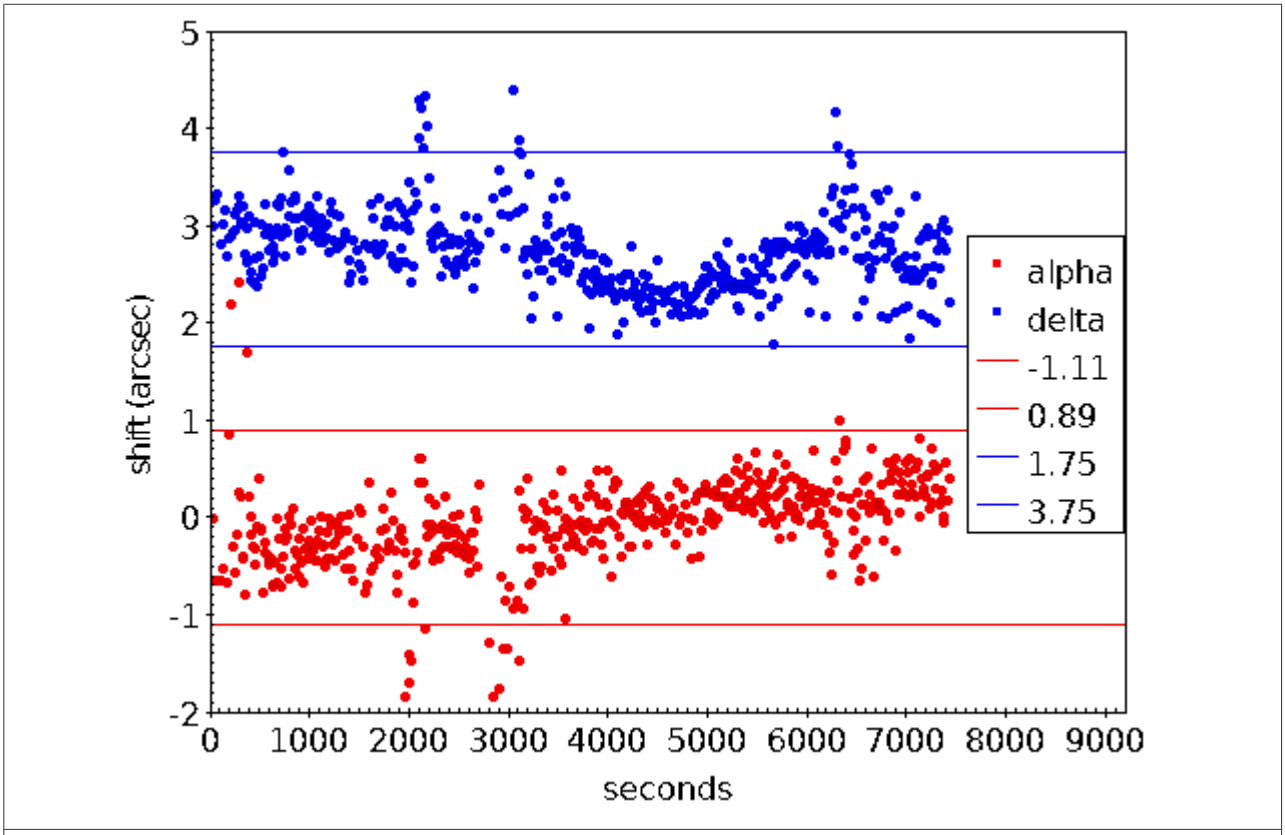

Fig. A30: typical expected drifting in alpha and delta directions. The slit width is shown as the horizontal blue and red double lines. Punctual departure in the guiding where due to passing clouds inducing the loss of the guiding star.